

# A 3D Diffusive and Advective Model of Electron Transport Applied to the Pulsar Wind Nebula HESS J1825-137

T. Collins,<sup>1\*</sup>, G. Rowell<sup>1</sup>, F. Voisin<sup>1</sup>, S. Einecke<sup>1</sup>, Y. Fukui<sup>2</sup> and H. Sano<sup>3</sup>

<sup>1</sup>*School of Physical Sciences, University of Adelaide, Adelaide 5005, Australia*

<sup>2</sup>*Department of Physics, University of Nagoya, Furo-cho, Chikusa-ku, Nagoya, 464-8601, Japan*

<sup>3</sup>*Faculty of Engineering, Gifu University, Yanagido 1-1, Gifu, 501-1193, Japan*

Accepted XXX. Received YYY; in original form ZZZ

## ABSTRACT

HESS J1825-137 is one of the most powerful and luminous TeV gamma-ray pulsar wind nebulae (PWNe), making it an excellent laboratory to study particle transportation around pulsars. We present a model of the (diffusive and advective) transport and radiative losses of electrons from the pulsar powering HESS J1825-137 (PSR 1826-1334) using interstellar medium gas (ISM) data, soft photon fields and a spatially varying magnetic field due to the pulsar. Assuming a characteristic age of 21 kyr, PSR 1826-1334 is unable to meet the energy requirements to match the observed X-ray and gamma-ray emission. An older age of 40 kyr requiring 14% of the pulsar’s spin-down power and advective flow with a velocity of  $v = 0.002 c$  towards lower Galactic longitudes is able to produce an asymmetric gamma-ray morphology and the multi-wavelength spectral energy distribution towards HESS J1825-137. In addition, a turbulent ISM with magnetic field of  $B = 20 \mu\text{G}$  to  $60 \mu\text{G}$  to the north of HESS J1825-137 (as suggested by ISM observations) is required to prevent significant gamma-ray contamination towards the northern TeV source HESS J1826-130.

**Key words:** cosmic rays - ISM: evolution - gamma-rays: general - X-rays: general - ISM individual (HESS J1825-137) - pulsars: individual (PSR J1826-1334)

## 1 INTRODUCTION

HESS J1825-137 is a luminous pulsar wind nebula (PWN) powered by pulsar PSR 1826-1334 with spin-down power  $\dot{E} = 2.8 \times 10^{36} \text{ erg s}^{-1}$  and characteristic age  $\tau_c = P/2\dot{P} = 21.4 \text{ kyr}$  (Aharonian et al. 2005b; Manchester et al. 2005). The distance to PSR J186-130 has been estimated to lie at a distance of  $\approx 4.0 \text{ kpc}$  based on dispersion measurements (Taylor & Cordes 1993; Cordes & Lazio 2002). The TeV gamma-ray emission from HESS J1825-137 has characteristic  $(1/e)$  extension of  $0.66^\circ \pm 0.03^\circ_{\text{stat}} \pm 0.04^\circ_{\text{sys}}$ , implying a radius of  $\approx 46 \text{ pc}$  based on a distance of  $4.0 \text{ kpc}$  (H.E.S.S. Collaboration et al. 2019). Owing to its brightness in TeV gamma rays, HESS J1825-137 is an ideal laboratory to study relativistic particle transportation in and around middle-aged PWNe. Several studies (e.g. Porth et al. (2016), Giacinti et al. (2020)) suggest that both diffusive and advective transport mechanisms is required to explain the extended gamma-ray morphology towards PWNe.

Situated  $0.7^\circ$  north of HESS J1825-137 (see Figure 1), HESS J1826-130 is a TeV gamma-ray source and possible accelerator of cosmic rays up to PeV energies (HAWC Collaboration et al. 2019; Cao et al. 2021). Due to its close proxim-

ity to HESS J1825-137, HESS J1826-130 was originally considered an extension of HESS J1825-137 until it revealed it was a separate source of gamma rays (H.E.S.S. Collaboration et al. 2018a; Aharonian et al. 2005a). Two supernova remnants (SNRs) (SNR G018.1-0.1 and SNR G018.6-0.2) lie in the vicinity of HESS J1826-137 (Odegard 1986; Brogan et al. 2006). However, their offset positions and small angular diameters make it unlikely that they are connected to the gamma-ray emission (H.E.S.S. Collaboration et al. 2020). The Eel PWN (PWN G18.5-0.4) and PSR J1826-1256 are associated with HESS J1826-130 based on spatial coincidence (H.E.S.S. Collaboration et al. 2018a). PSR J1826-1256 has a spin-down power of  $3.6 \times 10^{36} \text{ erg s}^{-1}$  and characteristic age of 14 kyr, well within the range of pulsar properties associated with TeV PWNe (Manchester et al. 2005; H.E.S.S. Collaboration et al. 2018b).

Araya et al. (2019) revealed GeV gamma-ray emission  $\sim 2.5^\circ$  to the Galactic south of HESS J1825-137. The same study postulated that the GeV emission from this region originates from cosmic rays accelerated by the SNR or PWN associated with HESS J1825-137 or a star forming region such as the Cygnus Cocoon. Spectral energy distribution (SED) modelling towards the GeV region suggests that the emission may be reflective of an earlier epoch of the PWN or a combination of HESS J1825-137 and nearby compact object LS 5039 (Collins et al. 2021).

\* E-mail: tiffany.collins@adelaide.edu.au

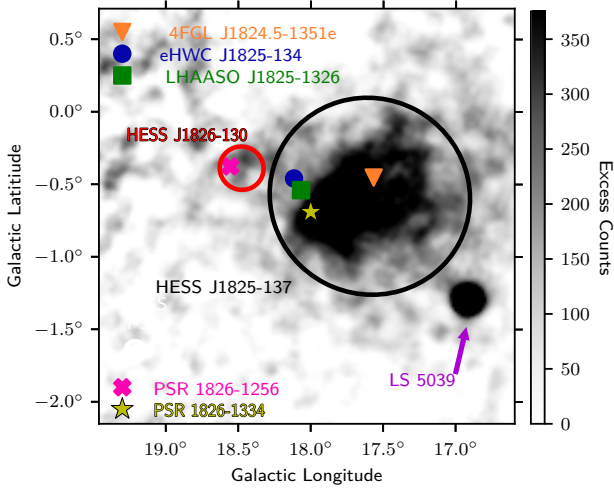


**Figure 1.** HESS excess count map towards HESS J1825-137 (H.E.S.S. Collaboration et al. 2019) overlaid by the regions used to extract the gamma-ray spectra towards HESS J1825-137 (black) and HESS J1826-130 (red). The positions of PSR J1826-1256 and PSR J1826-1334 are shown together with 4FGL J1824.5-1351e (radius= 0.75°), eHWC J1825-134 (radius= 0.36°) and LHAASO J1825-1326 (radius= 0.3°).

The PWN associated with HESS J1825-137 is expanding within the progenitor SNR. A large H $\alpha$  rim-like structure discovered by Stupar et al. (2008) is present towards the south of HESS J1825-137. Voisin et al. (2016) postulated a connection between this rim and another southern H $\alpha$  rim to the progenitor SNR of HESS J1825-137. Both structures lie  $\approx 1.7^\circ$  away from PSR 1826-1334 ( $\approx 120$  pc for a distance of 4 kpc), which is consistent with the predicted SNR radius of  $\approx 130$  pc as suggested by de Jager & Djannati-Ataï (2009).

The evolution of the cosmic-ray energy distribution can be described by the Fokker-Planck equation for particle transport (e.g. (Skilling 1975; Cesarsky & Volk 1978)). Henceforth, this equation will be called the transport equation for simplicity. Analytical solutions of the transport equation can be found for specific cases, e.g. an impulsive source in a homogeneous environment (Blumenthal & Gould 1970; Atoyan et al. 1995; Aharonian & Atoyan 1996), however, it must be solved numerically for more complex systems, e.g. continuous source where cosmic-ray propagation and radiative losses vary strongly with position.

Many models of HESS J1825-137 and other environments assume an homogeneous nebula; where high-energy electrons are injected into a symmetric sphere of constant density and magnetic field (e.g. H.E.S.S. Collaboration et al. (2019); Principe et al. (2020)). For example, the work conducted by Van Etten & Romani (2011) treated the transport of electrons from the powering pulsar as a series of uniform, spherical ‘bubbles’ and projected the gamma-ray SED onto a 2D plane. But the asymmetric gamma-ray morphology towards HESS J1825-137 noted by H.E.S.S. Collaboration et al. (2019) suggests a similarly irregular particle density and/or magnetic field around the pulsar.

Our study in this paper numerically solves the transport equation over a 3D Cartesian grid based on Voisin (2017). The spatially-dependent hydrogen number density and magnetic field for each voxel (a 3D pixel) in the grid follows observations of the ISM. The transport of high-energy electrons from PSR J1826-1334 is modelled in order to reproduce the X-ray and gamma-ray morphology, SED and radial profiles towards HESS J1825-137.

## 2 PARTICLE TRANSPORT AND RADIATIVE LOSSES

Upon the release of cosmic rays from an accelerator, such as a SNR or PWN, particles are transported throughout the ISM and experience radiative losses. The number distribution evolution of particles (cosmic-ray protons and electrons),  $n = n(\gamma, \mathbf{r}, t)$ , with Lorentz factor  $\gamma$  in neutral ISM containing inhomogeneous magnetic fields can be described by (e.g. Skilling (1975); Cesarsky & Volk (1978)):

$$\frac{\partial n}{\partial t} = -\nabla \cdot (n\mathbf{v}_A) - \nabla \cdot (\overline{\overline{D}} \cdot \nabla n) + \frac{\partial}{\partial \gamma} (\dot{\gamma} n) - \frac{1}{3} \frac{\partial}{\partial \gamma} (\gamma (\nabla \cdot \mathbf{v}_A)) n + \frac{\partial}{\partial \gamma} \left( \gamma^2 D_{\gamma\gamma} \frac{\partial}{\partial \gamma} \left( \frac{n}{\gamma^2} \right) \right) + S(\gamma, \mathbf{r}, t) \quad (1)$$

The first term in Equation 1 describes the evolution of cosmic-ray density due to advection as a co-moving fluid with velocity  $\mathbf{v}_A = \mathbf{v}_A(\gamma, \mathbf{r}, t)$ . The second term considers the spatial diffusion of cosmic rays as a second rank tensor ( $\overline{\overline{D}} = \overline{\overline{D}}(\gamma, \mathbf{r}, t)$ ); allowing preferential direction of transport. The third term considers losses due to radiative processes and adiabatic expansion. The fourth term represents diffusion resulting from re-acceleration of cosmic rays due to stochastic processes with  $D_{\gamma\gamma}$  being the acceleration rate (e.g. Tsytoich (1966)). Finally  $S(\gamma, \mathbf{r}, t)$  is the cosmic ray source/injection function.

To numerically solve Equation 1, the region of interest was divided into a grid of voxels of with dimensions  $\Delta x \Delta y \Delta z$ . Figure F1 shows a 2D representation of this grid. Finite difference techniques were used to transfer electrons in and out of each cell over time step  $\Delta t$  to model the transport. The following discussion describes how the implemented model treats individual terms in Equation 1.

### 2.1 Diffusion

Over distances smaller than the gyro-radius,  $r_g$ , electrons propagate through the ISM via ballistic motion. In a medium with randomised magnetic turbulence ( $\delta B$ ), electrons scatter and the motion switches to a diffusive regime for distances larger than the gyro-radius (e.g. Prosekin et al. (2015)). For a simple case of isotropic diffusion, the diffusion tensor in Equation 1 becomes a scalar;  $\overline{\overline{D}} \rightarrow D(E, B)$ , where  $E$  is the energy of the cosmic ray and  $B$  is the magnetic field.

Suppression of cosmic-ray diffusion is to be expected towards PWNe and SNRs where magnetic field turbulence is enhanced and the diffusion coefficient,  $D(E, B)$ , can be parameterized by (e.g. Gabici et al. (2007)):

$$D(E, B) = \chi D_0 \left( \frac{E/\text{TeV}}{B/3 \mu\text{G}} \right)^\delta \quad [\text{cm}^2 \text{s}^{-1}] \quad (2)$$

where  $D_0 = 3 \times 10^{27} \text{ cm}^2 \text{s}^{-1}$  is the average Galactic diffusion coefficient at 1 GeV,  $\delta = 0.5$  (in the Kraichnan regime) and the diffusion suppression factor  $\chi$  takes values  $\leq 1$  (Berezinskii et al. 1990). Gabici et al. (2007) found that highly suppressed diffusion ( $\chi \sim 0.01$ ) in molecular clouds can significantly effect the shape of the observed gamma-ray spectrum. The diffusion suppression factor is poorly constrained, but is demonstrated by studies towards SNR W28. Li & Chen (2010), Giuliani et al. (2010) and Gabici et al. (2010) found  $\chi = 0.1, 0.01$  and  $0.06$  respectively. Similarly, Protheroe et al. (2008) showed that the suppression factor towards the star forming region Sgr B2 takes values  $< 0.02$  based on the

radio synchrotron flux. Modelling by H.E.S.S. Collaboration et al. (2019) suggests that towards HESS J1825-137 the Galactic diffusion coefficient takes a value of  $D_0 = 1.4 \times 10^{29} \text{ cm}^2 \text{ s}^{-1}$  at 1 TeV.

The diffusive component of Equation 1 can be described using finite difference techniques:

$$n_{\text{diff}} \left| \frac{\gamma}{t + \Delta t} \right|_{x, y, z} = \sum_{\{i=x, y, z\}} \left[ \mathcal{D} \left| \frac{\gamma}{t + \Delta t/2} \right| \left( n \left| \frac{\gamma}{t - \Delta t} \right|_{i + \Delta i} - n \left| \frac{\gamma}{t} \right|_i \right) + \mathcal{D} \left| \frac{\gamma}{t + \Delta t/2} \right| \left( n \left| \frac{\gamma}{t} \right|_{i - \Delta i} - n \left| \frac{\gamma}{t} \right|_i \right) \right] \quad (3)$$

where electrons from the current time step,  $n(\gamma, t)$ , are first allowed to radiatively cool and are then incremented with the net transfer of electrons from the surrounding voxels.  $\gamma_0$  describes the Lorentz factor at time  $t$  before electrons cool to factor  $\gamma$  at time  $t + \Delta t$  and  $\mathcal{D} = D(\gamma, B)\Delta t/\Delta x^2$  is a dimensionless diffusion factor with  $D(\gamma, B)$  being the diffusion coefficient from Equation 2.

By solving Equation 1 for simple isotropic diffusion and accounting for radiative losses in the environment around accelerators, the electron energy distribution in each voxel of the 3D grid is tracked until the age of the system is reached. The subsequent multi-wavelength photon SED, radial profiles and morphology can then be predicted for the regions of interest.

The implemented model tracks the particle motion from voxel to voxel in a 3D grid. As a result, each time step must ensure that electrons travel a maximum displacement less than the size of the voxel. By knowing that  $n > 0$  and for Lorentz Factor  $\gamma$ , the  $x, y, z$  position of the maximum value of  $\mathcal{D}$  remains constant over time:

$$n_{\text{max}}(1 - 6\mathcal{D}) \geq n_{\text{max}}\mathcal{D} \quad (4a)$$

$$\mathcal{D} \leq \frac{1}{7} \quad (4b)$$

where the factor of 6 in Equation 4a comes about from the Cartesian configuration. The time step is dependent on the voxel size  $\Delta i = \Delta x = \Delta y = \Delta z$ :

$$\Delta t = \frac{\Delta i^2}{\mathcal{D}_{\text{max}}} \quad (5)$$

where  $\mathcal{D}_{\text{max}}$  is the maximum value of  $\mathcal{D}$  across the 3D grid.

## 2.2 Advection

The advective component of Equation 1 is given by:

$$\left( \frac{\partial n}{\partial t} \right)_{\text{adv}} = -\nabla \cdot (n\mathbf{v}_A) \quad (6)$$

where  $\mathbf{v}_A$  is the velocity due to the bulk flow of electrons. For simplicity,  $\mathbf{v}_A$  was assumed to be spatially and energy independent across the 3D Cartesian grid. Using the finite difference method as described in subsection 2.1, Equation 6 could be solved numerically via:

$$\left( \frac{\partial n}{\partial t} \right)_{\text{adv}} \left| \frac{\gamma}{t + \Delta t} \right|_{x, y, z} = -v \frac{\Delta t}{\Delta x} \left\{ \begin{aligned} n_{i+\Delta i}^t - n_i^t, & \quad v_i < 0 \\ n_i^t - n_{i-\Delta i}^t, & \quad v_i > 0 \end{aligned} \right. \quad (7)$$

where  $v_i$  is the component of advective velocity in the  $x, y$  and  $z$  direction. Equation 7 uses the forward difference method to approximate the derivative in Equation 6 when  $v_i < 0$  and the backward difference method when  $v_i > 0$ . Note that isotropic diffusion with an advective velocity can be approximated as anisotropic diffusion.

For Equation 7 to numerically model the transport of electrons due to advection, the time step must be chosen so that an electron does not travel across more than one voxel in time  $\Delta t$ :

$$\Delta i \geq |v|\Delta t \quad (8)$$

## 2.3 Radiation Losses

High-energy electrons interact with the ISM via inverse Compton interactions on ambient photons, via Bremsstrahlung with interstellar gas and via synchrotron interactions against magnetic fields (see Appendix. A). The evolution of the electron number density with Lorentz factor  $\gamma$  due to radiative losses is given by:

$$\frac{\partial n}{\partial t} = \frac{\partial}{\partial \gamma} (\dot{\gamma} n) \quad (9)$$

where the cooling rate,  $\dot{\gamma}(\gamma)$ , is given by Manolakou et al. (2007):

$$\dot{\gamma}(\gamma) = b_s \gamma^2 + b_c (3 \ln \gamma + 18.8) + 5.3 b_b + \sum_{i=1} b_{\text{IC}}^i \gamma^2 F_{\text{KN}}^i(\gamma) \quad (10)$$

for the case of ionisation or Bremsstrahlung losses in neutral hydrogen. Here,  $i$  sums over all radiation fields (CMB, Infra-red and optical photons),  $b_s, b_c, b_b$  and  $b_{\text{IC}}$  are the coefficients for synchrotron losses, Coulomb losses, Bremsstrahlung losses and inverse Compton losses respectively and  $F_{\text{KN}}$  is the Klein-Nishina cross section (see Equation A6). The general solution to Equation 9 is:

$$n(\gamma, t + \Delta t) = \frac{\dot{\gamma}_0}{\dot{\gamma}} n(\gamma_0, t) \quad (11)$$

with  $n(\gamma_0, t)$  being the initial energy distribution with Lorentz factor  $\gamma_0$  at time  $t = t$ .

## 2.4 Adiabatic expansion and re-acceleration of electrons

For an energy independent advective velocity  $\mathbf{v}_A$ , losses due to adiabatic expansion is given by:

$$\frac{\partial n}{\partial t} = -\frac{1}{3} (\nabla \cdot \mathbf{v}_A) n \quad (12)$$

Due to the assumption that advection is spatially independent, adiabatic losses were not considered. Moreover, studies such as Tanaka & Takahara (2010) and Porth et al. (2016) that considered spherically symmetric advection concluded that adiabatic losses are dominant over radiation losses for low energy electron ( $< 10$  TeV). Therefore, losses due to adiabatic expansion are not considered here but are left for future work.

The termination shock (TS) of pulsars have been proposed as sites for re-acceleration of electrons through diffusive shock acceleration (DSA). The source term in Equation 2 treats the injected electron spectrum as the spectra obtained after re-acceleration due to the TS by ensuring the voxel size  $\Delta x \Delta y \Delta z$  is larger than the radius of the TS ( $r_{\text{ts}} = 0.1$  pc). Furthermore, magnetohydrodynamics

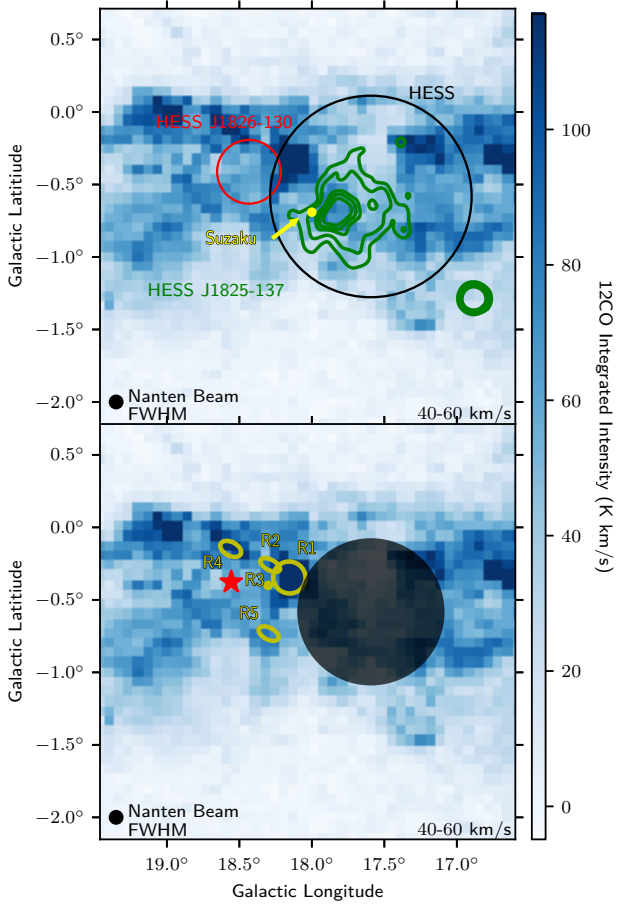


**Figure 2.** (top) Nanten  $^{12}\text{CO}(1-0)$  integrated intensity in the velocity range  $40 - 60 \text{ km s}^{-1}$  corresponding to  $3.5 - 4.5 \text{ kpc}$  overlaid by green H.E.S.S. contours (at 4, 5, 6, 7, 8 and  $9 \sigma$ ). The yellow circle represents the X-ray region A as defined in Uchiyama et al. (2009). The region used to obtain the gamma-ray spectra towards HESS J1825-137 and HESS J1826-130 are shown in black and red respectively. (bottom) The voxels in black are set to a density of  $0.5 \text{ cm}^{-3}$  to represent the bubble that has been swept out by the stellar wind from the progenitor star. Molecular clouds R1-R5 from Voisin et al. (2016) are shown in yellow with the position of PSR J1826-1256 indicated by the red star.

models (e.g. Lemoine & Pelletier (2010); Sironi et al. (2015)) suggest that DSA at the TS is too suppressed for electron acceleration up to energies responsible for the TeV emission seen towards PWN. Hence, the re-acceleration of electrons (fifth term in Equation 2) will not be concluded.

### 3 APPLICATION TO HESS J1825-137

The modelling described in section 2 was then applied to the PWN HESS J1825-137.

#### 3.1 The environment towards HESS J1825-137

##### 3.1.1 Gas morphology, Magnetic Field and Soft Photon Fields

Our model tracked the particle transport over a 3D grid of interstellar medium (ISM) gas with each voxel containing a value for the ISM gas density. Using the Nanten  $^{12}\text{CO}(1-0)$  survey (Mizuno & Fukui

**Table 1.** Parameters describing molecular hydrogen/ISM gas towards HESS J1825-137 and HESS J1826-130 (see Figure 2) using Nanten  $^{12}\text{CO}(1-0)$  data.

Object	$M_H (M_\odot)$	$n_H (\text{cm}^{-3})$	Radius (arcmin)
HESS J1825-137	$1.86 \times 10^6$	170	42
HESS J1826-130	$3.13 \times 10^4$	195	10

2004), the total column density of molecular hydrogen,  $N_{H_2}$ , was traced towards the region of interest using

$$N_{H_2} = X_{12\text{CO}} W_{12\text{CO}} \quad (13)$$

where  $W_{12\text{CO}}$  is the integrated intensity of the gas.  $X_{12\text{CO}} = 1.5 \times 10^{20} \text{ cm}^{-2} \text{ K}^{-1} \text{ km}^{-1} \text{ s}$  is assumed to be constant over the Galactic plane but may vary with galactocentric radius (Strong et al. 2004). The locality of HESS J1825-137 allows the assumption of a constant  $X_{12\text{CO}}$  towards the region of interest. PSR 1826-1334 has a dispersion measure distance of  $3.9 \pm 0.4 \text{ kpc}$  (Taylor & Cordes 1993), thus ISM data in the velocity range of  $40 - 60 \text{ km s}^{-1}$  was considered (Voisin et al. 2016). This is equivalent to distances of  $3.5 \text{ kpc}$  to  $4.5 \text{ kpc}$  as given by the Galactic rotation model (Brand & Blitz 1993). Atomic hydrogen in the same velocity range contributes less than 1% to the total column density towards HESS J1825-137 and was not considered (Voisin et al. 2016; Collins et al. 2021).

Each voxel in the 3D grid (see Figure F1) has a volume of  $\Delta x \Delta y \Delta z$  where  $\Delta z$  is the voxel length in the line of sight. For the purposes of this study, we utilised a  $200 \text{ pc} \times 200 \text{ pc} \times 200 \text{ pc}$  grid consisting of voxels of size  $2 \text{ pc} \times 2 \text{ pc} \times 2 \text{ pc}$ . Assuming that all the gas in the  $40 - 60 \text{ km s}^{-1}$  velocity range lies within the 3D grid, Equation 14 calculated the density in each cubic voxel. The Nanten telescope has a velocity resolution of  $1 \text{ km s}^{-1}$  (Mizuno & Fukui 2004), therefore we assumed that density along the line of sight in the 3D grid is constant for simplicity. The number density of gas within a voxel with average column density of  $N_{H_2}$ , area  $A = \Delta x \Delta y$  and volume  $V = \Delta x \Delta y \Delta z$  was calculated by:

$$n_H = \frac{N_H}{\Delta z} \quad [\text{cm}^{-3}] \quad (14)$$

$N_H = 2.8 N_{H_2}$  considers a 20% He component. The mass of gas in each voxel is:

$$M_H = n_H V m_p \quad (15)$$

where  $m_p$  is the mass of a proton.

Figure 2 shows Nanten  $^{12}\text{CO}(1-0)$  integrated intensity in the  $40 - 60 \text{ km s}^{-1}$  range. The average molecular number densities towards HESS J1825-137 and HESS J1826-130 are given in Table 1

Stellar winds from the progenitor star of PSR J1826-1334 will push out gas in the nearby vicinity (Castor et al. 1975). The subsequent supernova explosion creates a ‘bubble’ of hot dense gas around a low-density interior. A region of low density gas in the  $40 - 60 \text{ km s}^{-1}$  velocity range can be seen towards the centre of the TeV emission in Figure 2. To include this, any voxels lying within the extent of the PWN volume (a sphere centered on the pulsar with radius  $0.5^\circ$ ) was set to a density of  $0.5 \text{ cm}^{-3}$  based on the average densities expected within massive stellar wind bubbles (Weaver et al. 1977).

Turbulent motion in interstellar medium results in an amplification of magnetic field, suppressing the diffusion of electrons as they travel through the ISM as given by Equation 2. Figure 6 of Voisin et al.

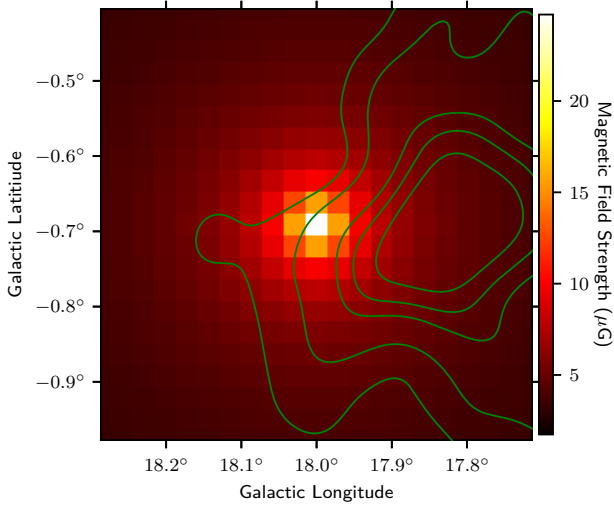


**Figure 3.** A 2D representation of the magnetic field due to the PWN with the pulsar centred on the origin. The magnetic field is related to the distance from pulsar through Equation 16. Overlaid are the green H.E.S.S. contours at 4, 5, 6, 7, 8 and 9  $\sigma$ .

(2016) shows a three coloured image of the CS(1-0) and  $\text{NH}_3$  integrated intensity between  $40-60 \text{ km s}^{-1}$  and the  $\text{H}62\alpha$  integrated intensity between  $45-65 \text{ km s}^{-1}$  towards the cloud defined as R1 (see Figure 2 for the position of clouds R1-R5 from Voisin et al. (2016)). Located between HESS J1825-137 and HESS J1826-130, cloud R1 is highly turbulent with minimum magnetic field strength of  $21 \mu\text{G}$  as given by Crutcher's relation (see Equation B1). Given the likely physical proximity of this turbulent ISM to HESS J1825-137, cloud R1 may act as a barrier for electrons escaping into HESS J1826-130 from PSR 1826-1334 (Voisin et al. 2016).

Following Van Etten & Romani (2011), the magnetic field due to the PWN was assumed to follow a time-independent power-law with a decreasing magnetic field strength varying with distance  $r$  from the pulsar:

$$B_{\text{PWN}}(r) = B_0 \left( \frac{r}{r_{\text{ts}}} \right)^{-\beta} \quad (16)$$

where  $r_{\text{ts}} = 0.03 \text{ pc}$  is the radius of the termination of shock, and  $B_0$  and  $\beta$  are free parameters chosen to match the X-ray and gamma-ray spectra of HESS J1825-137. Van Etten & Romani (2011) suggests  $\beta = -0.69$  for an age of 40 kyr. Note that Van Etten & Romani (2011) considers an additional dependence on the spin-down energy of the pulsar which is not considered in this study for simplicity.

Crutcher's relation (see Equation B1) suggests that the magnetic field contribution of gas with number density  $\leq 300 \text{ cm}^{-3}$  is  $10 \mu\text{G}$ . As PWNe are expected to evolve inside a low dense bubble formed by stellar winds from the progenitor, only the magnetic field due to the pulsar will initially be considered.

The photon fields around HESS J1825-137 are estimated utilising the radiation field model described by Popescu et al. (2017); the Far-infrared field (FIR) with temperature  $T = 40 \text{ K}$  and energy density  $U = 1 \text{ eV cm}^{-3}$ , near infra-red field (NIR) with temperature  $T = 500 \text{ K}$  and energy density  $0.4 \text{ eV cm}^{-3}$  and optical light with temperature  $T = 3500 \text{ K}$  and energy density of  $U = 1.9 \text{ eV cm}^{-3}$  (these are similar to the values utilised by Van Etten & Romani (2011), who assumed a FIR field of  $U = 1 \text{ eV cm}^{-3}$  with  $T = 32 \text{ K}$  and optical field of  $U = 4 \text{ eV cm}^{-3}$  with  $T = 2500 \text{ K}$ ).

### 3.1.2 Evolution of electron injection

Cosmic rays (and high energy electrons) injected into the 3D grid at the position of PSR J1826-1334 ( $\ell = 18.0^\circ$  and  $b = -0.69^\circ$ ) and follow an exponential cutoff power-law:

$$S(E, t) = A \left( \frac{E}{1 \text{ TeV}} \right)^{-\Gamma} \exp \left( -\frac{E}{E_c} \right) \quad (17)$$

where  $E_c$  is the cutoff energy and  $A$  is the normalisation factor. For PWN, we assume that point-like particle injection is powered by the spin-down power,  $\dot{E}$ , of the associated pulsar:

$$\dot{E}(t) = \int S(E, t) dE \quad (18)$$

At time  $t$  the spin-down power of the pulsar is given by (see Appendix D):

$$\dot{E}(t) = \dot{E}(t_{\text{age}}) \left[ 1 + (n-1) \frac{\dot{P}(t - t_{\text{age}})}{P} \right]^{-\Gamma_n} \quad (19)$$

where  $n$  is the braking index of the pulsar with  $\Gamma_n = (n+1)/(n-1)$  and  $\dot{E}(t_{\text{age}})$ ,  $P$  and  $\dot{P}$  are the spin-down power, period and spin-down period of the pulsar at the current age  $t_{\text{age}}$ .

## 3.2 Results

As the `Multizone` model allows variation over numerous parameters (e.g. electron injection spectra, ISM parameters, ect.), a single-zone model was utilised to gain insight into HESS J1825-137 before more complex modelling. Single zone modelling takes a region of uniform number density and magnetic field to model the multi-wavelength SED. The results of the single-zone modelling is shown in Appendix. C. For an age of 21 kyr, the single-zone model required electrons to follow an exponential cutoff power-law with spectral index  $\Gamma = 2.1$  and cutoff  $E_c = 40 \text{ TeV}$  to match the gamma-ray SED while an older age of 40 kyr required index of  $\Gamma = 2.1$  and cutoff  $E_c = 50 \text{ TeV}$ .

### 3.2.1 Model 1 - Isotropic Diffusion

PWNe are formed by winds generated by a pulsar. By the time electrons reach the termination shock of the pulsar ( $\approx 0.1 \text{ pc}$ ), multiple scattering events have randomised the direction of motion. Hence, this study first considered a simple model of isotropic diffusion.

Based on the results of the single-zone model, `Multizone` was used to model the electron energy density towards HESS J1825-137. Electrons were injected by PSR J1826-1334 according to an exponential cutoff power-law spectra ( $\frac{dN}{dE} \propto E^{-\Gamma} \exp(E/E_c)$ ) and then transported by methods described in section 2. The time step used for the finite difference technique is  $\approx 7 \text{ yr}$ . These electrons interact with the soft photon and magnetic fields to produce gamma rays (see Appendix. A). Two different ages of 21 kyr and 40 kyr were considered following Van Etten & Romani (2011).

Figure 4 and Figure 5 shows the modelled gamma-ray morphology in different energy bands, the multiwavelength SED and the 1–9 keV X-ray and 0.1–91 TeV gamma-ray radial profiles for the 21 and 40 kyr models respectively as well as corresponding model inputs. To compare the modelled gamma-ray radial profile to observations, a collection area of  $0.25 \text{ km}^2$  was used (Benbow 2005) for an observation time of 387 hr as utilised by H.E.S.S. Collaboration



et al. (2019). Similarly a collection area of  $0.029 \text{ m}^2$  was utilised to compare the modelled X-ray profile to the observed Suzaku radial profile shown in Figure 4 from Uchiyama et al. (2009). Figure 6 shows the modelled SED towards HESS J1826-130 due to electrons escaping from HESS J1825-137 for the 40 kyr model.

Both ages predicted that the gamma-ray morphology towards HESS J1825-137 is symmetric around the powering pulsar with some gamma-ray contribution  $< 1 \text{ TeV}$  via Bremsstrahlung radiation toward the region between HESS J1825-137 and HESS J1826-130 (see Figure 4 and Figure 5). The 40 kyr gamma-ray emission between  $1 - 10 \text{ TeV}$  extends further from the pulsar than the 21 kyr emission. Both ages predicted a steep radial profile for X-rays between  $1 - 9 \text{ keV}$  (see the left lower-middle right panels of Figure 4 and Figure 5). The 21 kyr model was able to replicate the HESS radial profile for gamma rays between  $0.133 - 91 \text{ TeV}$  (see the right lower-middle panel of Figure 4) while the 40 kyr model over-predicted the gamma-ray emission for distances  $> 0.5^\circ$  from the pulsar (see the lower-middle right panel of Figure 5).

The 21 kyr modelled gamma-ray SED was able to match observations with a slight over-prediction ( $\sim 94\%$ ) of the HESS data between  $1 - 10 \text{ TeV}$  as seen in the single-zone models (see Figure C1). While able to predict the normalisation of X-rays produced by synchrotron emission, the model was unable to replicate the slope of the observed Suzaku SED. The 40 kyr SED was able to predict both the X-ray and gamma-ray SED with a similar over-prediction in  $1 - 10 \text{ TeV}$  photons as seen in the 21 kyr model. A slight ‘bump’ is present in the SED for photons around  $50 - 100 \text{ TeV}$  for both ages.

The 21 kyr model required electrons with spectral index  $\Gamma = 2.0$  and cutoff  $40 \text{ TeV}$  to be injected into the ISM with injection luminosity  $3.0 \times 10^{37} \text{ erg s}^{-1}$ . This exceeds the spin-down power of PSR 1826-1334 by a factor of 10. The 40 kyr model had an electron injection luminosity of  $4.0 \times 10^{35} \text{ erg s}^{-1}$  ( $\approx 14\%$  of  $\dot{E}_{\text{PSR}}$ ) with spectral index and cutoff of  $1.9$  and  $500 \text{ TeV}$  respectively. Consequently, in our model we will only consider an age of 40 kyr.

The observed gamma-ray contamination of HESS J1826-130 by HESS J1827-137 was estimated by H.E.S.S. Collaboration et al. (2020) to be  $\approx 40\%$  for photon energies below  $1.5 \text{ TeV}$  and  $20\%$  above  $1.5 \text{ TeV}$ . The modelled SED towards HESS J1826-130 can therefore be used to further constrain the model. The SED towards HESS J1826-130 is extracted from the red source region shown in Figure 2 and is defined in § 3.2 of H.E.S.S. Collaboration et al. (2020). The gamma-ray SED towards HESS J1826-130 due to HESS J1825-137 at age 40 kyr is shown in Figure 6 together with the spectrum of HESS J1826-130 and equivalent *Fermi*-LAT source 4FGL J1826.1-1256. The residuals are given by:

$$\text{Residual} = \frac{f_{\text{J1826}} - f_{\text{model}}}{f_{\text{J1826}}} \quad (20)$$

where  $f_i = E^2 \frac{dN_i}{dE}$  ( $i = \text{J1826 or model}$ ) for the SED observed towards HESS J1826-130 and the predicted SED from the model. For photons below  $2 \text{ TeV}$ , the SED towards HESS J1826-130 as a result of HESS J1825-137 exceeds observations. In the model, too many low energy electrons have escaped into the region towards HESS J1826-130 before losing their energy to radiative losses. It is clear that further refinement of the model is required to accurately describe the region surrounding HESS J1825-137.

### 3.2.2 Model 2 - Isotropic Diffusion + Advection

The gamma-ray morphology in Figure 5 shows that Model 1 40 kyr (isotropic diffusion) did not predict the extended TeV gamma-ray morphology towards HESS J1825-137 at lower Galactic longitudes (see blue the arrow in the upper-middle left panel of Figure 5). H.E.S.S. Collaboration et al. (2019) suggested that particle transport within the PWN is a combination of diffusion and an additional advective flow of electrons with a total flow velocity of  $0.01c$ . Thus, Model 2 introduced an advective flow.

The modelled flux, radial profiles and gamma-ray morphology for Model 2 40 kyr with an advective flow of  $v = 0.002$  are shown in Figure 7. A comparison between different advection speeds ( $v = 0.001c$ ,  $v = 0.002c$  and  $v = 0.003c$ ) is shown in Figure F5.

For further comparison of the morphology towards HESS J1825-137, slices were taken across the model maps and compared to the HESS data. The results and the region used to take the slices are shown in Figure 8. An advective velocity of  $0.002c$  was chosen so that the peak in the modelled gamma-ray morphology in energy range  $E < 1 \text{ TeV}$  and  $1 \text{ TeV} < E < 10 \text{ TeV}$  corresponds to the HESS data (see the left-upper panel of Figure F5).

While an additional advective flow lowered the gamma-ray SED towards HESS J1826-130 for energies less than  $2 \text{ TeV}$ , the emission still exceeds H.E.S.S. observations.

### 3.2.3 Model 3 - Isotropic Diffusion + Advection + Magnetic Field towards HESS J1826-130

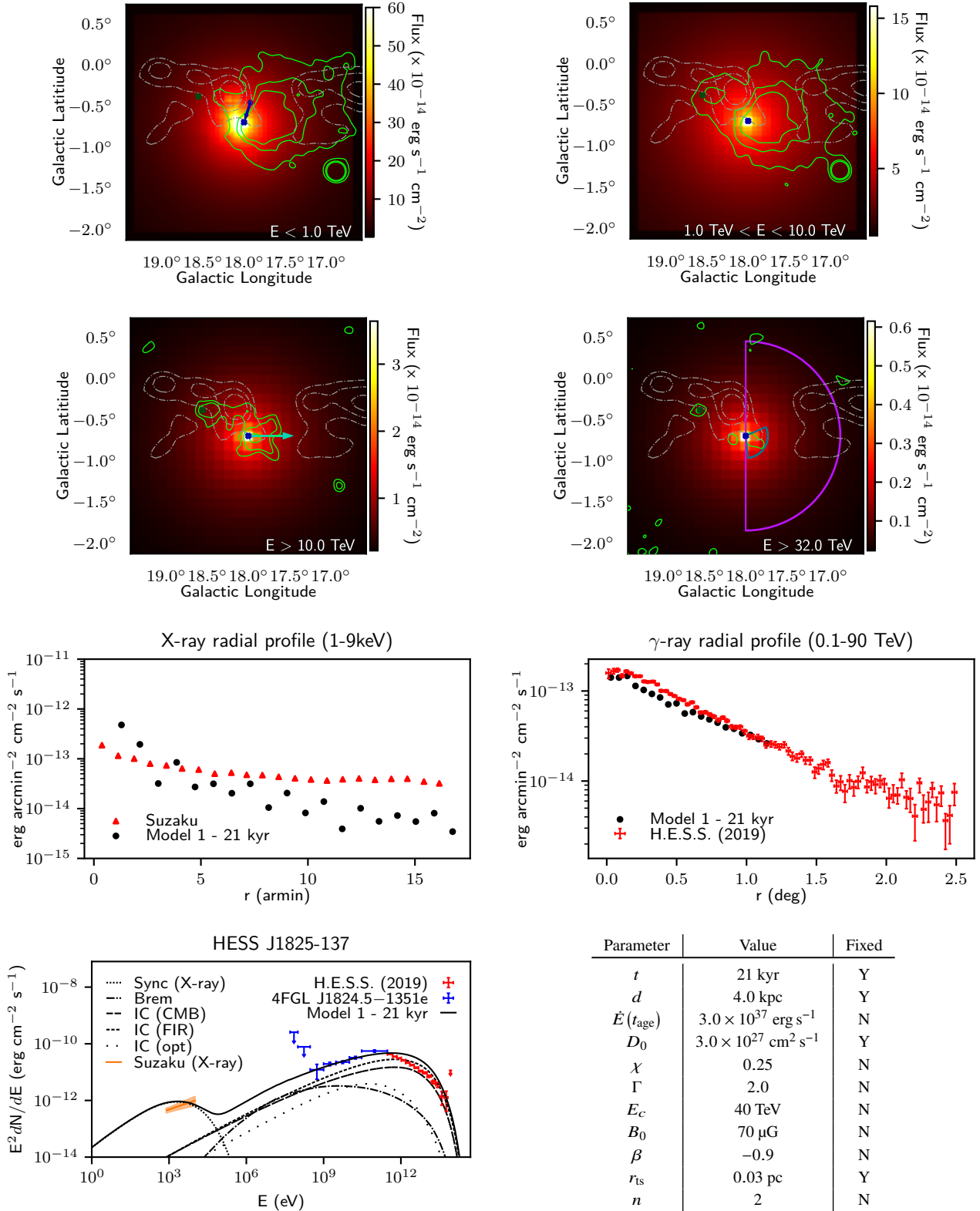
As discussed in § 3.1.1, the turbulent molecular gas between HESS J1825-137 and HESS J1826-130 can act as a barrier for electrons escaping from the PWN. As clouds R1-R5 are positioned in an approximate semi-circle around PSR J1826-1256 (see Figure 2), Model 3 considered a shell of dense gas centred on HESS J1826-130 with inner and outer radii  $0.17^\circ$  and  $0.33^\circ$  respectively with an advective velocity of  $v_A = 0.002c$ .

Figure 9 shows the SED, radial profiles and gamma-ray slices of HESS J1825-137 and HESS J1826-130 for Model 3 with magnetic field strengths of  $B = 20, 60$  and  $100 \mu\text{G}$ . A comparison between the 40 kyr Model 1, isotropic diffusion + magnetic field of  $60 \mu\text{G}$  (Model 3\*) and Model 3  $60 \mu\text{G}$  is shown in Figure 10 as well as the gamma-ray morphology for Model 3. All models have the same parameters as Model 1 40 kyr that is detailed in the table of Figure 5.

## 3.3 Discussion

### 3.3.1 Model 1 - Isotropic Diffusion

The 21 kyr and 40 kyr models were unable to reproduce both the X-ray and gamma-ray radial profiles. For example, the diffusion suppression coefficient,  $\chi$ , could be increased to compensate for the steep X-ray radial profile for the 21 kyr model. Electrons would then escape the PWN at a higher rate and the gamma-ray radial profile will flatten. This can be seen in the 40 kyr model, which assumes a lower value of  $\chi$  than the 21 kyr model. The shallow 40 kyr gamma-ray radial profile indicates that lower energy electrons have started to accumulate near the pulsar, while high-energy electrons rapidly lose their energy through radiative cooling and do not escape far from the pulsar. This is demonstrated in the upper right panel in Figure 5 where the gamma-ray flux below  $10 \text{ TeV}$  is relatively constant over the grid while the flux above  $10 \text{ TeV}$  is constrained to the pulsar. This accumulation is not as apparent in the 40 kyr X-ray radial profile



**Figure 4.** 21 kyr Model 1 - Isotropic diffusion. (Top & Middle Upper) Modelled gamma-ray morphology towards HESS J1825-137 in different energy band overlaid by green HESS significance contours (5, 10 and 15 $\sigma$  for  $E < 10$  TeV and 3, 5 and 10 $\sigma$  for  $E > 10$  TeV) and grey 40, 50 and 60 $\sigma$  Nanten  $^{12}\text{CO}$  integrated intensity contours. PSR 1826-134 and PSR 1826-1256 are shown by the dark blue and green crosses respectively. The direction of advection flow as discussed by H.E.S.S. Collaboration et al. (2019) is shown by the light blue arrow for  $E > 10$  TeV. The current proper motion direction of PSR 1826-1334 is indicated by the dark blue arrow for  $E < 1$  TeV with its projected birth place shown by the empty blue circle (based on age 21 kyr). The regions used to obtain the X-ray and gamma radial profiles are shown as the dark blue and purple wedges respectively in the  $E > 32$  TeV. Middle Lower - Left 1 – 9 keV X-ray radial profile in comparison to Suzaku (Uchiyama et al. 2009). Middle Lower - Right 0.1 – 91 TeV gamma-ray radial profile compared to red HESS observations (H.E.S.S. Collaboration et al. 2019). Bottom - Left Modelled SED towards HESS J1825-137 compared against the orange Suzaku X-ray spectral fit, 4FGL J1824.5-1351e flux points (blue) and HESS J1825-137 SED (red). Bottom - Right Corresponding model parameters.

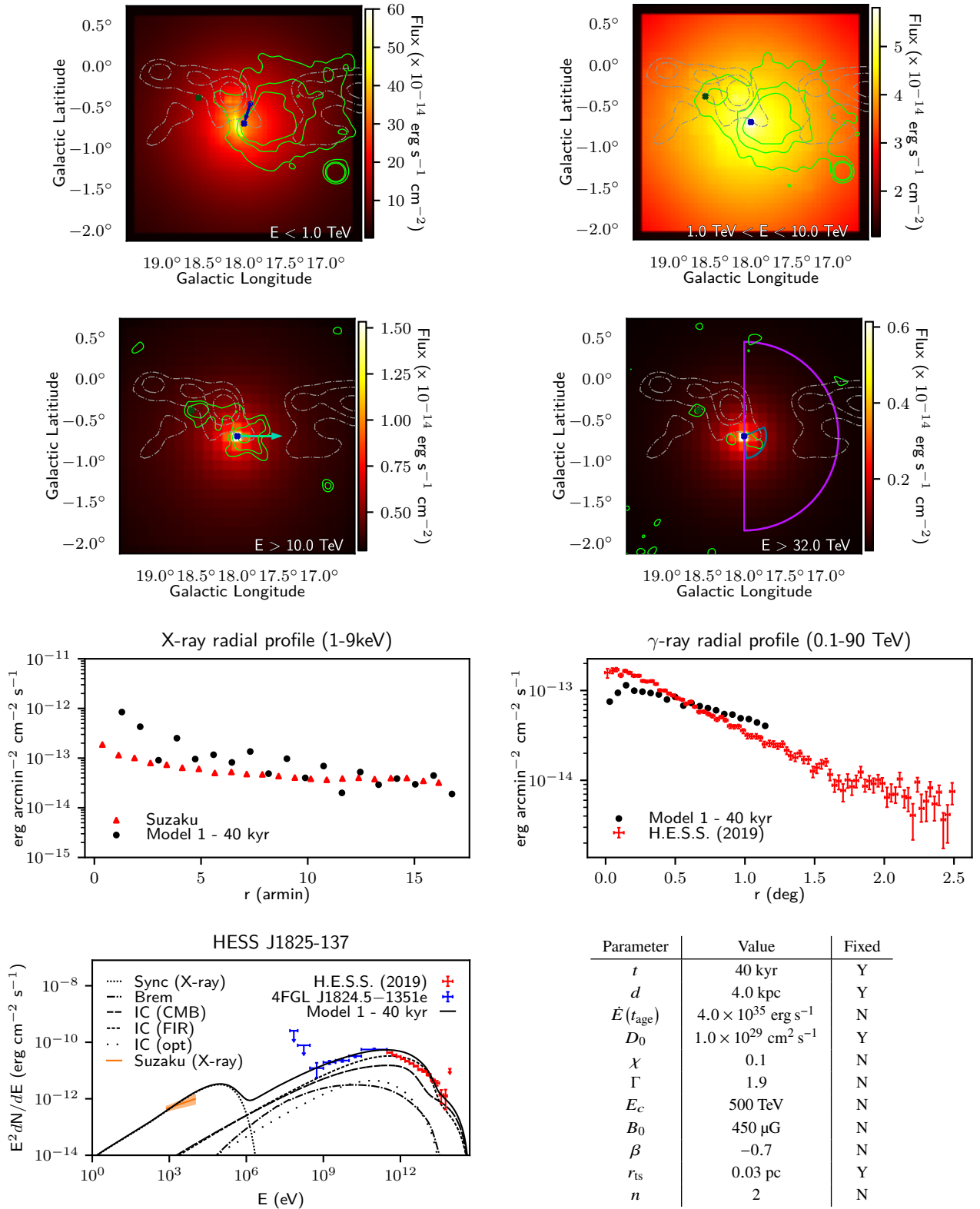


**Figure 5.** 40 kyr Model 1 - Isotropic diffusion. Same panel layout as in Figure 4. The projected birth place based on age 40 kyr is shown by the empty blue circle.



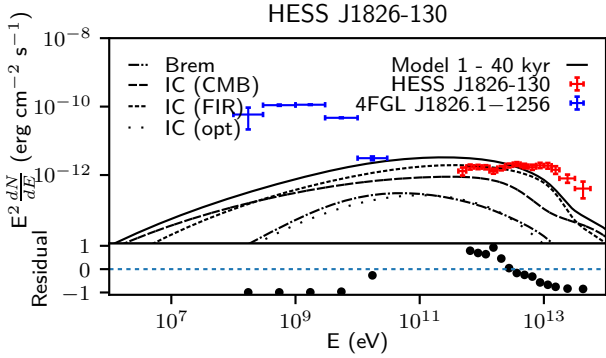


**Figure 6.** Total SED (solid black line) towards HESS J1826-130 (using the region encapsulated by the red circle in Figure 2) from electrons accelerated by PSR 1826-1256 by the 40 kyr Model 1. The GeV and TeV gamma-ray flux points towards HESS J1826-130 are represented by blue and red respectively. The bottom panel shows the residuals of the model as given by Equation 20

and the SED as the regions used in extracting X-ray spectra and radial profile are smaller than the regions used for the gamma-ray analysis (see Figure 2 and upper-middle right panel of Figure 4). The accumulation of lower-energy electrons is also reflected as a bump in the TeV gamma-ray SED. The bump occurs when synchrotron losses start to dominate at electron energies  $> 9$  TeV, resulting in inverse Compton radiation  $> 6$  TeV (Manolakou et al. 2007; Hinton & Hofmann 2009). This bump is not present for a slightly younger age of 36 kyr as the 40 kyr) as shown in Figure F2. The higher energy TeV emission at age 36 kyr matches the 40 kyr emission while the GeV and lower energy TeV emission is weaker for 36 kyr.

The 21 kyr model required an electron injection luminosity of  $3.0 \times 10^{37} \text{ erg s}^{-1}$ , exceeding the spin-down power of PSR 1826-1334 ( $\dot{E} = 2.8 \times 10^{36} \text{ erg s}^{-1}$ ). A higher braking index results in a greater quantity of electrons at earlier times (see Equation 19), reducing the current spin-down power of the pulsar. This results in an accumulation of electrons at lower energy, consequently increasing the gamma-ray flux for photons with energies  $< 1$  TeV (see Figure F3). Similarly the accumulation of electrons increases the X-ray flux for lower photon energies ( $E < 1 \text{ keV}$ ). This suggests that the age of HESS J1825-137 lies between 21 kyr and 40 kyr. The 40 kyr magnetic field profile takes values of  $B_0 = 450 \mu\text{G}$  and  $\beta = -0.7$  (see Equation 16) in comparison to  $B_0 = 400 \mu\text{G}$  and  $\beta = -0.69$  used in (Van Etten & Romani 2011). Van Etten & Romani (2011) considered an evolving magnetic field  $B \propto \dot{E}(t)$  where the magnetic field takes larger values at earlier times. This could explain the larger  $B_0$  normalisation used in our modelling.

### 3.3.2 Model 2 - Isotropic Diffusion + Advection

An advective component of  $0.002c$  towards lower Galactic longitudes was included into Model 2.

The SED and X-ray radial profile with an advective transportation component remains unchanged to Model 1 40 kyr (as shown in the lower-middle and lower-left panels of Figure 7. Electrons rapidly escape the small ( $r = 0.05^\circ$ ) X-ray region, hence the subsequent X-ray SED and radial profile depends more on the injected electron spectra rather than the method of transport. On the other hand, for both Model 1 and Model 2, the majority of electrons remain within the large ( $0.7^\circ$ ) HESS region leaving the gamma-ray

SED unchanged. However, the electrons in Model 2 have migrated further from the pulsar while remaining within the HESS region. Subsequently, the gamma-ray profile for Model 2 is flatter than Model 1 (lower-middle right panel of Figure 7).

Figure F4 shows the distance that electrons are transported before losing their energy to radiation. It can be seen that advection is the dominant particle transport method for electron energies less than 10 TeV, resulting in IC emission below 1 TeV. Diffusion is dominant for electrons above 10 TeV. However, these high-energy electrons do not travel far from their birthplace before losing their energy to radiative cooling.

The peak in the uncorrelated excess slices is offset from the position of the pulsar as described by H.E.S.S. Collaboration et al. (2019). Our model assumes that the position of the pulsar does not change over its lifetime. However, any kick velocity gained by the pulsar during the progenitor supernova will shift the source of electrons over time. Old, low-energy electrons will then appear to originate in a position offset to the current position of the pulsar while young, high-energy electrons appear to originate at the pulsar (Principe et al. 2020). The direction of proper motion of PSR 1826-1334 is shown by the cyan arrow in the left upper-middle panel of Figure 4, Figure 5 and Figure 7 and lies parallel to the region used to construct the slice morphology in Figure 8. At all energies, the gamma-ray slices for Model 1 appears symmetric around the pulsar position and shows no preferential direction of transportation. However, the HESS uncorrelated excess data indicates that electrons are preferential transported to lower Galactic longitudes. With the addition of an advective flow of  $0.002c$ , the peak in the 40 kyr gamma-ray slices for photons less than 1 TeV is now offset from the pulsar and follows the shape of the uncorrelated excess. For the  $1 \text{ TeV} < E < 10 \text{ TeV}$  energy band, both Model 1 and Model 2 show a flatter slice profile compared to HESS observations. Electrons resulting from this emission appear to be contained near their birthplace before escaping into the nebula.

Our model assumes that the diffusion index,  $\chi$ , lies within the Kraichnan regime ( $\delta = 0.3 - 0.6$ ) with the index being fixed at  $\delta = 0.5$ . The top-right panel of Figure 8 shows that the modelled gamma-ray slice morphology is broader than that observed by HESS, suggesting that electrons are constrained within the PWN. This suggests that the diffusion index inside the PWN may be somewhat less than the  $\delta = 0.5$  value we assumed, and perhaps to the lower bound for the Kraichnan regime.

By assuming that diffusion was isotropic in (as used in Equation 1), any preferential direction for particle transport was a result of ISM irregularities or advective flow. The highly asymmetric morphology towards HESS J1825-137 could be explained if diffusion is anisotropic with preferential diffusion towards lower Galactic longitudes. However, an anisotropic diffusion model can be approximated by an isotropic diffusion + advection model (Model 2).

### 3.3.3 Model 3 - Isotropic Diffusion + Advection + Magnetic Field towards HESS J1826-130

Here, a spherical shell of increased magnetic field strength around HESS J1826-130 was considered to replicate the turbulent gas towards cloud R1 from Voisin et al. (2016).

The bottom-right panel of Figure 8 shows that cloud R1 lies within the area used to determine the gamma-ray SED of HESS J1825-137. The ratio of synchrotron to inverse Compton flux is proportional to the magnetic field (Aharonian et al. 1997). Hence, as the magnetic field around HESS J1826-130 increases, electrons lose more energy through synchrotron losses and the inverse Comp-

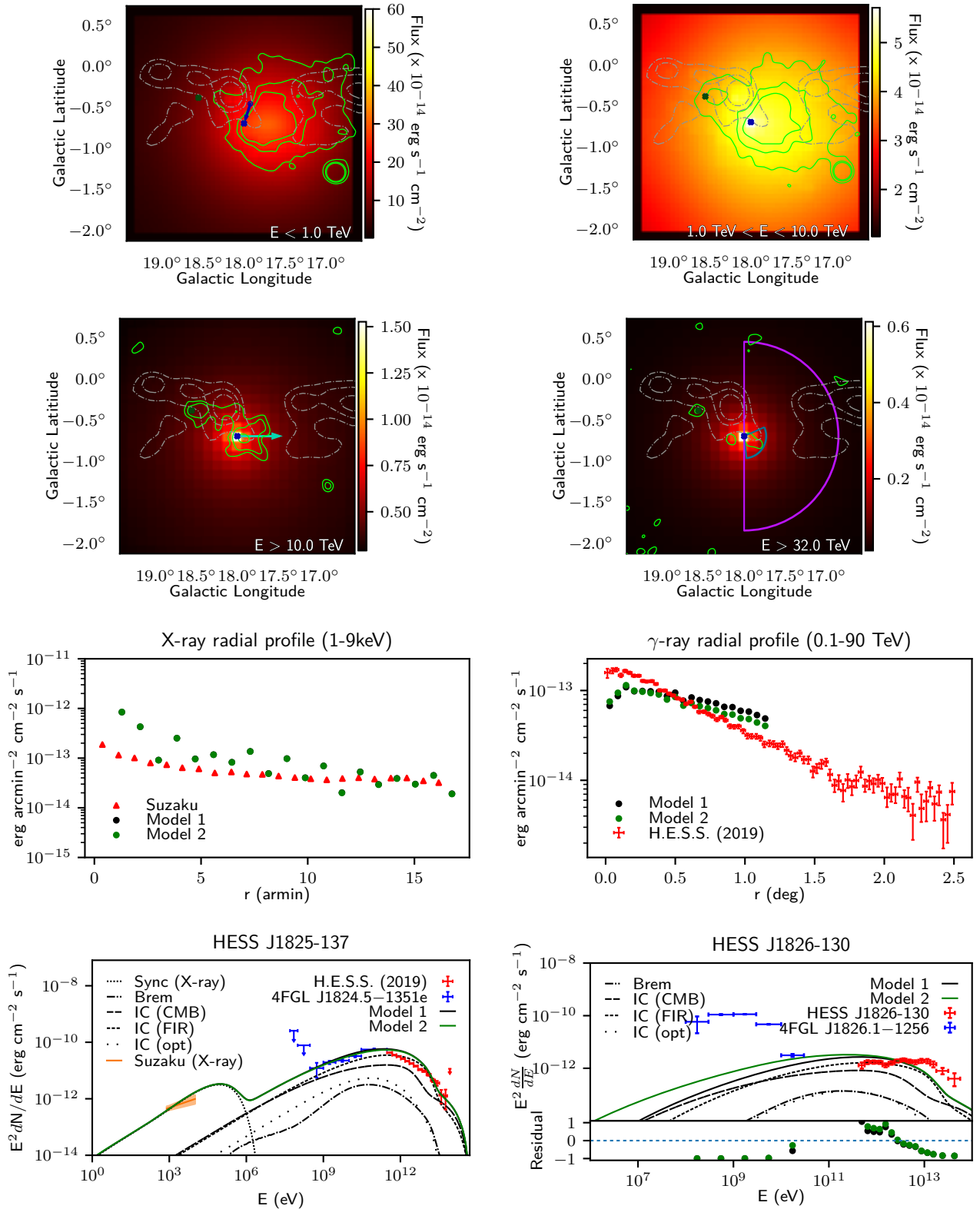


**Figure 7.** 40 kyr Model 2 - isotropic diffusion + advection ( $v = 0.002c$ ) with the same panel layout as in Figure 4. The total multi-wavelength SED and radial profiles for the diffusion + advection model is shown in green while the original diffusion model is shown in black.

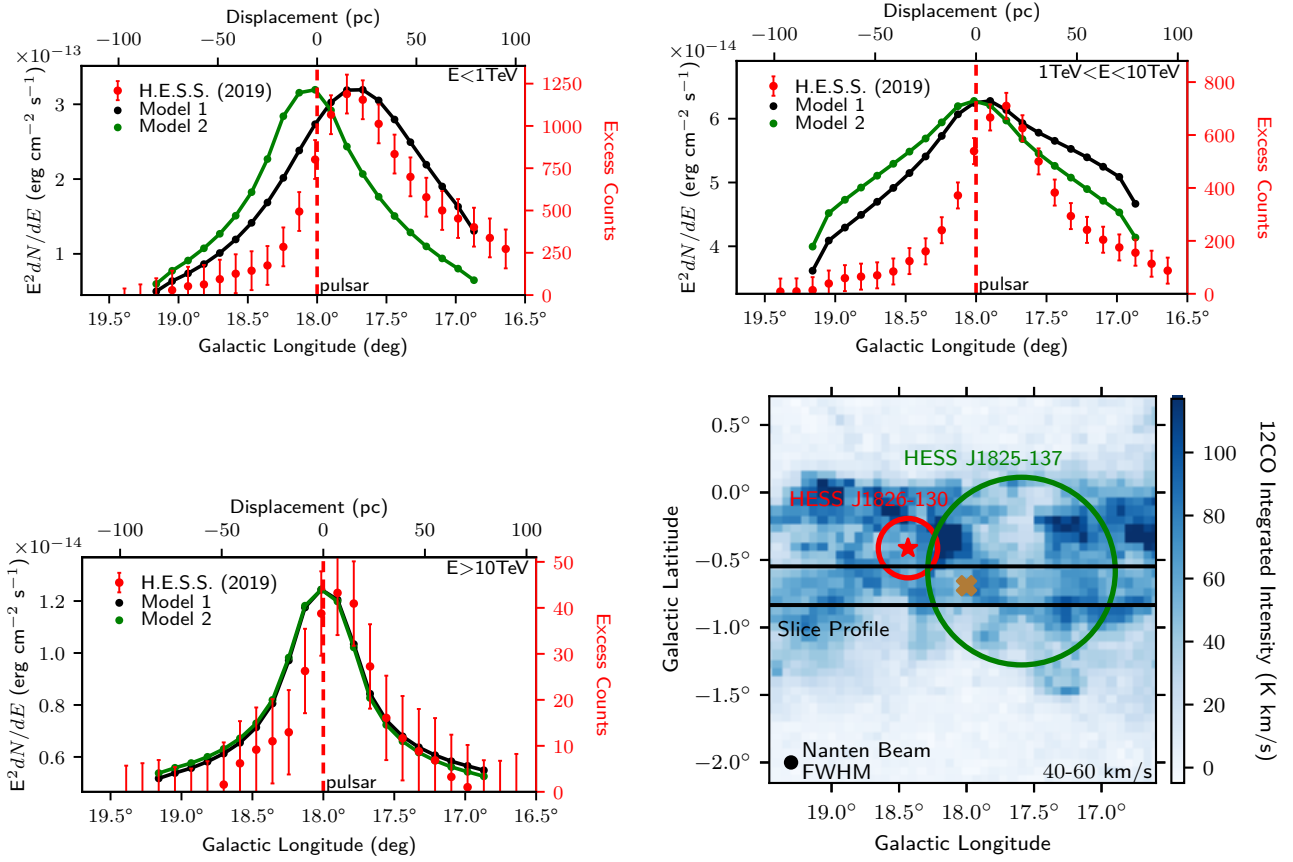


**Figure 8.** Slices taken along Galactic longitude with Model 1 (isotropic diffusion (black)) and Model 2 (isotropic diffusion + advection (green)) models at 40 kyr for energy bands  $E < 1$  TeV (top left),  $1 < E < 10$  TeV (top right) and  $E > 10$  TeV (bottom left) vs the H.E.S.S. data (H.E.S.S. Collaboration et al. 2019). The peak of Model 2 slices are normalised to the Model 1 slices. (bottom left) Nanten <sup>12</sup>CO(1-0) gas towards HESS J1825-137 in the 40 – 60 km s<sup>-1</sup> velocity band. The region used to take the slice profile is indicated by the black rectangle and the position of PSR 1826-1334 is marked by the orange cross.

ton flux decreases at equivalent gamma-ray energies. This can be seen in the SED for HESS J1825-137 in the lower-middle right panel of Figure 9. This has the effect of improving the match (from 94% to 44% over-prediction) to HESS observations between 1 – 10 TeV compared to Model 1 and Model 2 as shown in the bottom-middle-left panel of Figure 10.

The gamma-ray slice profiles are shown in the top and top-middle panels of Figure 9. As the magnetic field around HESS J1826-130 increases, gamma-ray emission less than 1 < TeV and > 10 TeV remains unchanged at lower longitudes, with a decrease at higher longitudes. Between 1 TeV <  $E$  < 10 TeV, the gamma-ray slice profile drops off at a shallower rate compared to the HESS data at lower Galactic magnitudes. However the gamma-ray emission at higher longitudes, representing the area towards HESS J1826-130, increases proportionally with the magnetic field.

Additionally, the bottom-left panel of Figure 9 indicates that increasing the magnetic field strength around HESS J1826-130 lowers the contamination of HESS J1826-130 by the PWN associated with HESS J1825-137 for energies < 2 TeV. Regions of high magnetic field strength experience a slower rate of diffusion (see Equation 2) and high synchrotron losses. Hence regions of high magnetic field tend to ‘block’ cosmic rays from passing through. The model implies that a minimum magnetic field strength of 60  $\mu$ G is required to successfully lower the contamination of HESS J1826-130 according to H.E.S.S. observations. The bottom-right panel of Figure 9 shows the

multi-wavelength spectral distribution towards HESS J1826-130. An upper-limit to the X-ray emission towards HESS J1826-130 can be obtained using HEARSAC’s X-Ray background tool utilising ROSAT data (Sabol & Snowden 2019). The estimated synchrotron flux towards HESS J1826-130 combined with the ROSAT X-ray upper limit (obtained from the same region used to extract the SED of HESS J1826-130) implies a maximum magnetic field strength of  $\approx 20 \mu$ G around HESS J1826-130. This constraint violation suggests that the model is not fully encapsulating the transport of particle between PSR 1826-1334 and HESS 1826-130.

### 3.4 Future Work

Presently, Multizone only considers isotropic diffusion and does not account for diffusion parallel and perpendicular to the magnetic field (Drury 1983; Lazarian et al. 2023). The magnetic fields of PWN are believed to be toroidal in nature (Schmidt et al. 1979; Kothes et al. 2006), hence diffusion is expected to be suppressed perpendicular to the magnetic axis of the pulsar. Additionally, the recent detection of TeV halos (Abeysekara et al. 2017) implies that the region surrounding the the PWN experiences a higher diffusion suppression compared to the average Galactic diffusion coefficient (Schroer et al. 2023). While current models of particle transport suggest that advection dominates particle transport within the PWN and diffusion dominates at the edges, this could be described by two dif-

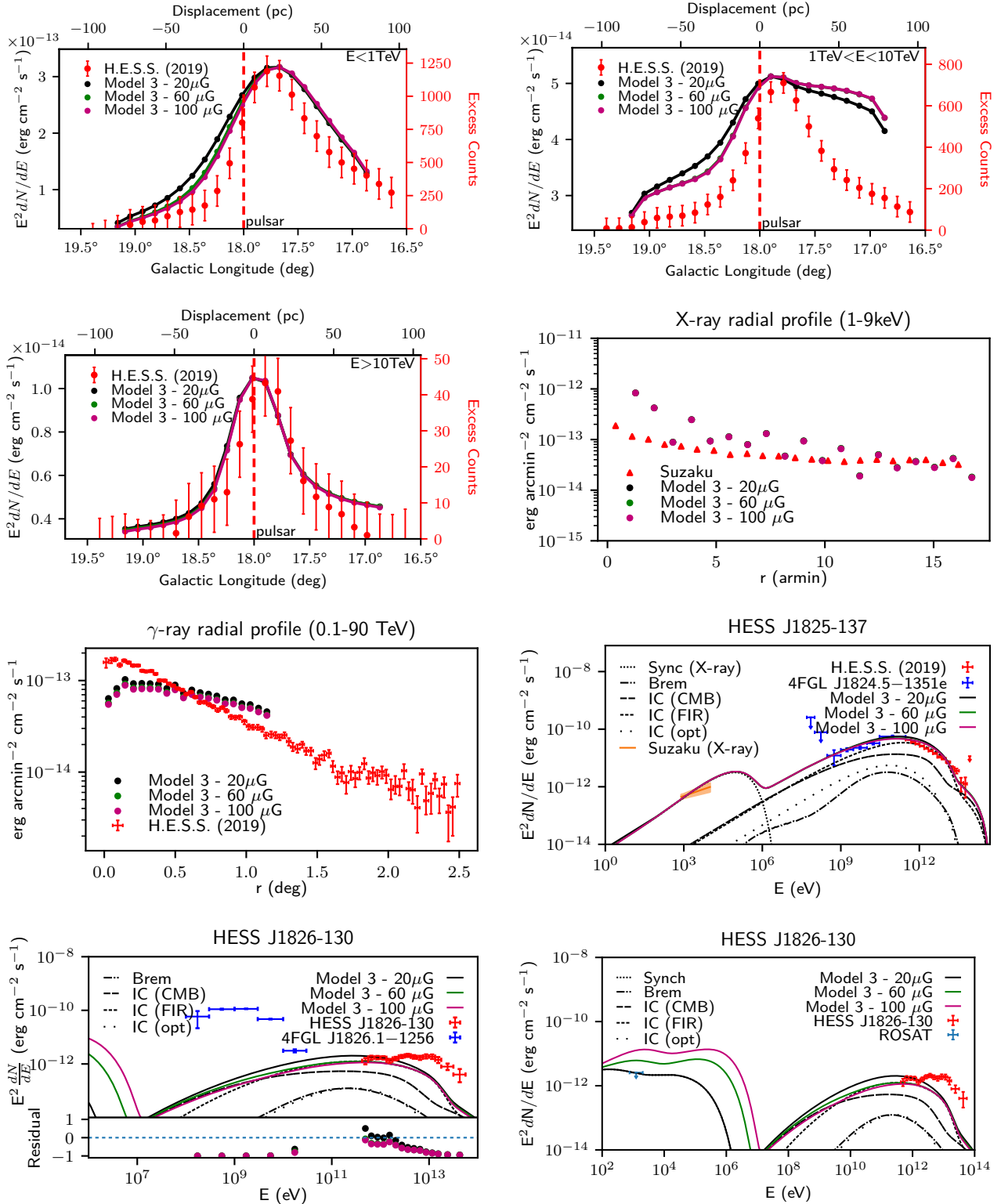


**Figure 9.** Model 3 - 40 kyr + advection + magnetic field of 20 μG (black), 60 μG (green) and 100 μG (purple) around HESS J1826-130.

ferent regions of diffusion suppression. Model 2 and 3 in this study considered spatially-independent advection towards lower Galactic longitudes to explain the asymmetric TeV gamma-ray morphology towards HESS J1825-137. As a result, losses due to adiabatic expansion were neglected. Any future modelling of PWN with Multi-

zone will investigate the effects of spatially-dependent anisotropic diffusion and an azimuthal and radial dependent advective velocity on the gamma-ray morphology and SED. This can then be applied to model the formation of the TeV halo around HESS J1825-137 (Principe et al. 2020).

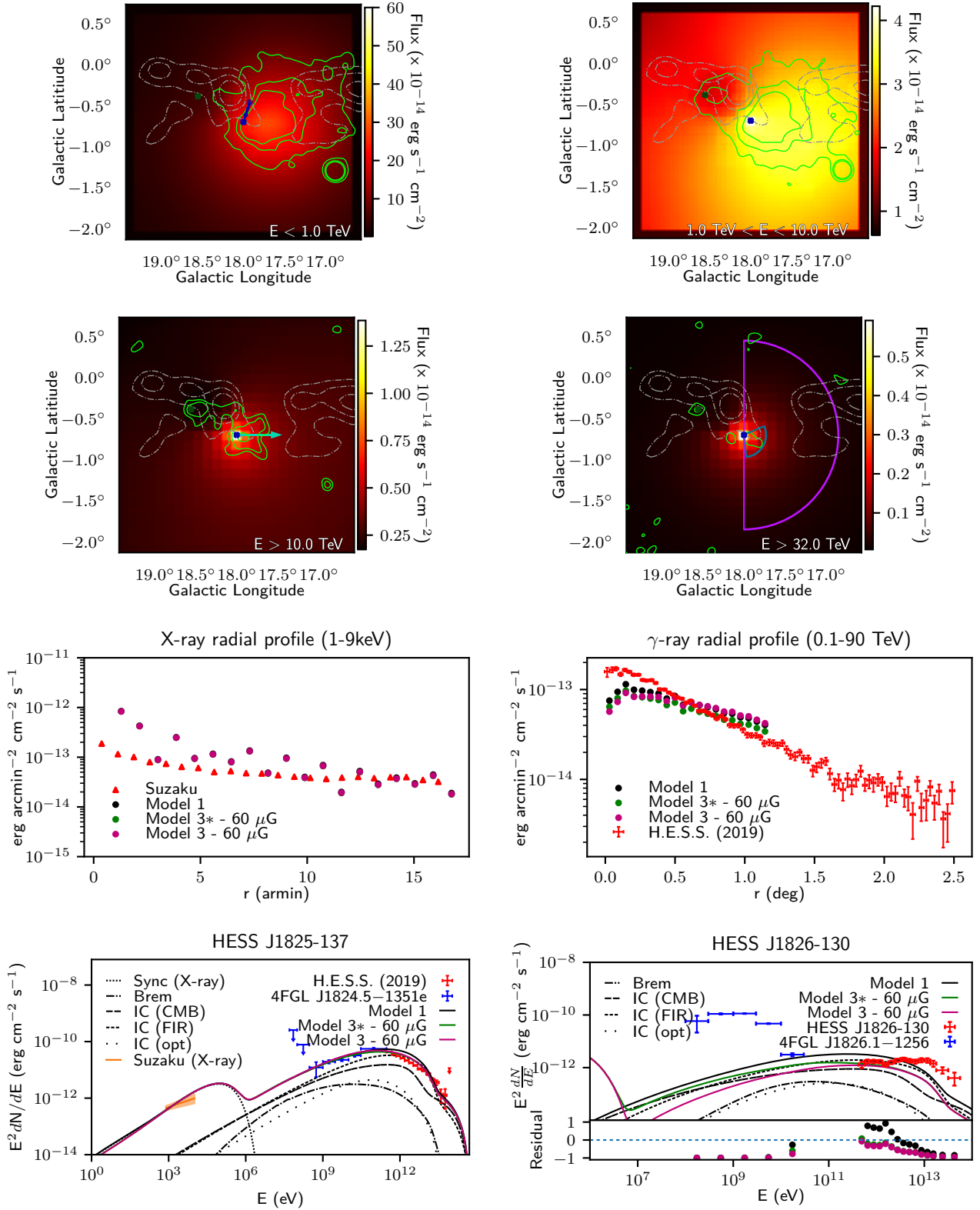


**Figure 10.** Comparison of the 40 kyr isotropic diffusion - Model 1 (black), isotropic diffusion + magnetic field of 60  $\mu\text{G}$  - Model 3\* (green) and the isotropic diffusion + advection + magnetic field of 60  $\mu\text{G}$  (purple) - Model 3. The morphology plots towards HESS J1825-137 for model 3 are shown in the top and upper middle panels.



The transverse velocity of PSR J1826-1334 ( $\approx 400 \text{ km s}^{-1}$ ) implies that the position of the pulsar has shifted approximately 9 pc and 16 pc for ages 21 kyr and 40 kyr respectively (Manchester et al. 2005). Multizone assumed that the position of the pulsar is constant over time which would not be the case for a voxel size of 2 pc. The implementation of a time-dependent source position would not affect the X-ray radial profile and SED due to the small extraction region and the pulsar's magnetic field (see Figure 3). However, the gamma-ray SED would remain unchanged as a result of the large HESS extraction region. Future work will investigate the affects of an evolving source position on the gamma-ray radial profile and morphology of HESS J1825-137. Similarly, the application of Multizone to SNRs would require cosmic rays to be injected by an expanding shell to model diffusive shock acceleration by the expanding SNR.

Multizone is not limited to HESS J1825-137 and can be used to model the transport of cosmic rays (electrons and protons) from other PWN and cosmic ray sources.

#### 4 SUMMARY

By modelling the transport of electrons across a 3D Cartesian grid of varying ISM density and magnetic field, we are able to predict the multi-wavelength emission and morphology towards HESS J1825-137. **Three models were considered; isotropic diffusion (Model 1), isotropic diffusion + advection (Model 2) and isotropic diffusion + advection + magnetic field towards HESS J1826-130 (Model 3).** The best fit 21 kyr and 40 kyr Model 1 consisted of a pulsar injecting electrons into the surrounding medium with injection luminosity of  $3.0 \times 10^{37} \text{ erg s}^{-1}$  and  $4.0 \times 10^{35} \text{ erg s}^{-1}$  respectively. This represents 1000% and 14% of the present spin-down power of the pulsar associated HESS J1825-137, indicating that the true age of the system is older than what the characteristic age suggests. While able to reproduce the multi-wavelength SED, neither model was able to perfectly reproduce the gamma-ray morphological profile described in H.E.S.S. Collaboration et al. (2019) for photons with energies  $1 \text{ TeV} < E < 10 \text{ TeV}$ . However, the morphological profile could be matched for gamma-rays with energies  $< 1 \text{ TeV}$  (with an offset of  $0.3^\circ$  towards higher Galactic longitudes compared to the HESS data) and energies  $> 10 \text{ TeV}$ .

Applying an advective bulk flow (with velocity  $v = 0.002 c$ ) of electrons towards lower Galactic longitudes did not alter the photon SED predicted by Model 1. By taking slices along the predicted flux maps, we were able to compare in detail the gamma-ray morphology towards HESS J1825-137. Model 2 40 kyr is able to reproduce the slice profile shape for photons  $< 1 \text{ TeV}$  and  $> 10 \text{ TeV}$ , however photons with energies  $1 < E < 10 \text{ TeV}$  experience a shallower drop-off compared to the uncorrelated HESS excess slices as revealed by H.E.S.S. Collaboration et al. (2019). This suggests that the parent electrons are constrained within the PWN before escaping into the interstellar medium to form a TeV halo.

As the gamma-ray emission associated with PSR 1826-1334 cannot exceed the observed emission towards HESS J1826-130, HESS J1826-130 can be used to constrain the model. Model 1 and Model 2 were found to over-predict the SED of HESS J1826-130 for photons  $< 1.5 \text{ TeV}$ . By placing a shell of increased magnetic field strength of at least  $60 \mu\text{G}$  around HESS J1826-130, representing the turbulent gas between the two HESS sources (Voisin et al. 2016), the contamination was successfully lowered below the levels closer to those estimated by HESS. By combining the modelled synchrotron

flux with the ROSAT X-ray upper limit towards HESS J1826-130, we were able to constrain the magnetic field shell to have maximum strength of  $20 \mu\text{G}$ . This constraint violation suggests that further modelling of the turbulent gas is needed to fully disentangle the particle transport towards HESS J1825-137.

#### ACKNOWLEDGEMENTS

T. Collins acknowledges support through the provision of Australian Government Research Training Program Scholarship.

The Nanten project is based on a mutual agreement between Nagoya University and the Carnegie Institution of Washington (CIW). We greatly appreciate the hospitality of all the staff members of the Las Campanas Observatory of CIW. We are thankful to many Japanese public donors and companies who contributed to the realization of the project.

This research has made use of the NASA's Astrophysics Data System and the SIMBAD data base, operated at CDS, Strasbourg, France.

#### DATA AVAILABILITY

No new data were generated or analysed in support of this research.

#### REFERENCES

- Abeyssekara A. U., et al., 2017, *Science*, 358, 911
- Aharonian F. A., Atoyan A. M., 1996, *A&A*, 309, 917
- Aharonian F. A., Atoyan A. M., Kifune T., 1997, *MNRAS*, 291, 162
- Aharonian F., et al., 2005a, *Science*, 307, 1938
- Aharonian F. A., et al., 2005b, *A&A*, 442, L25
- Araya M., Mitchell A. M. W., Parsons R. D., 2019, *MNRAS*, 485, 1001
- Atoyan A. M., Aharonian F. A., Völk H. J., 1995, *Phys. Rev. D*, 52, 3265
- Benbow W., 2005, in Aharonian F. A., Völk H. J., Horns D., eds, *American Institute of Physics Conference Series Vol. 745, High Energy Gamma-Ray Astronomy*. pp 611–616, doi:10.1063/1.1878471
- Berezinskii V. S., Bulanov S. V., Dogiel V. A., Ptuskin V. S., 1990, *Astrophysics of cosmic rays*. John Wiley & Sons, Inc.
- Blumenthal G. R., Gould R. J., 1970, *Reviews of Modern Physics*, 42, 237
- Brand J., Blitz L., 1993, *A&A*, 275, 67
- Brogan C. L., Gelfand J. D., Gaensler B. M., Kassim N. E., Lazio T. J. W., 2006, *ApJ*, 639, L25
- Cao Z., et al., 2021, *Nature*, 594, 33
- Castor J., McCray R., Weaver R., 1975, *ApJ*, 200, L107
- Cesarsky C. J., Volk H. J., 1978, *A&A*, 70, 367
- Collins T., Rowell G., Mitchell A. M. W., Voisin F., Fukui Y., Sano H., Alsulami R., Einecke S., 2021, *MNRAS*,
- Cordes J. M., Lazio T. J. W., 2002, *arXiv e-prints*, pp astro-ph/0207156
- Crutcher R. M., Wandelt B., Heiles C., Falgarone E., Troland T. H., 2010, *ApJ*, 725, 466
- Drury L. O., 1983, *Reports on Progress in Physics*, 46, 973
- Gabici S., Aharonian F. A., Blasi P., 2007, *Ap&SS*, 309, 365
- Gabici S., Casanova S., Aharonian F. A., Rowell G., 2010, in Boissier S., Heydari-Malayeri M., Samadi R., Valls-Gabaud D., eds, *SF2A-2010: Proceedings of the Annual meeting of the French Society of Astronomy and Astrophysics*. p. 313 (arXiv:1009.5291)
- Giacinti G., Mitchell A. M. W., López-Coto R., Joshi V., Parsons R. D., Hinton J. A., 2020, *A&A*, 636, A113
- Giuliani A., et al., 2010, *A&A*, 516, L11
- HAWC Collaboration et al., 2019, *arXiv e-prints*, p. arXiv:1909.08609
- H.E.S.S. Collaboration et al., 2018a, *A&A*, 612, A1
- H.E.S.S. Collaboration et al., 2018b, *A&A*, 612, A2
- H.E.S.S. Collaboration et al., 2019, *A&A*, 621, A116
- H.E.S.S. Collaboration et al., 2020, *A&A*, 644, A112

Hinton J. A., Hofmann W., 2009, ARA&A, 47, 523  
 Kothes R., Reich W., Uyaniker B., 2006, ApJ, 638, 225  
 Lazarian A., Xu S., Hu Y., 2023, Frontiers in Astronomy and Space Sciences, 10, 1154760  
 Lemoine M., Pelletier G., 2010, MNRAS, 402, 321  
 Li H., Chen Y., 2010, MNRAS, 409, L35  
 Manchester R. N., Hobbs G. B., Teoh A., Hobbs M., 2005, AJ, 129, 1993  
 Manolakou K., Horns D., Kirk J. G., 2007, A&A, 474, 689  
 Mizuno A., Fukui Y., 2004, in Clemens D., Shah R., Brainerd T., eds, Astronomical Society of the Pacific Conference Series Vol. 317, Milky Way Surveys: The Structure and Evolution of our Galaxy. p. 59  
 Odegard N., 1986, AJ, 92, 1372  
 Popescu C. C., Yang R., Tuffs R. J., Natale G., Rushton M., Aharonian F., 2017, MNRAS, 470, 2539  
 Porth O., Vorster M. J., Lyutikov M., Engelbrecht N. E., 2016, MNRAS, 460, 4135  
 Principe G., Mitchell A. M. W., Caroff S., Hinton J. A., Parsons R. D., Funk S., 2020, A&A, 640, A76  
 Prosekin A. Y., Kelner S. R., Aharonian F. A., 2015, Phys. Rev. D, 92, 083003  
 Protheroe R. J., Ott J., Ekers R. D., Jones D. I., Crocker R. M., 2008, MNRAS, 390, 683  
 Sabol E. J., Snowden S. L., 2019, xrbg: ROSAT X-Ray Background Tool, Astrophysics Source Code Library, record ascl:1904.001 (ascl:1904.001)  
 Sano H., et al., 2017, ApJ, 843, 61  
 Schmidt G. D., Angel J. R. P., Beaver E. A., 1979, ApJ, 227, 106  
 Schroer B., Evoli C., Blasi P., 2023, arXiv e-prints, p. arXiv:2305.08019  
 Sironi L., Keshet U., Lemoine M., 2015, Space Sci. Rev., 191, 519  
 Skilling J., 1975, MNRAS, 172, 557  
 Strong A. W., Moskalenko I. V., Reimer O., Digel S., Diehl R., 2004, A&A, 422, L47  
 Stupar M., Parker Q. A., Filipović M. D., 2008, MNRAS, 390, 1037  
 Tanaka S. J., Takahara F., 2010, ApJ, 715, 1248  
 Taylor J. H., Cordes J. M., 1993, ApJ, 411, 674  
 Tsytoich V. N., 1966, Soviet Physics Uspekhi, 9, 370  
 Uchiyama H., Matsumoto H., Tsuru T. G., Koyama K., Bamba A., 2009, PASJ, 61, S189  
 Van Etten A., Romani R. W., 2011, ApJ, 742, 62  
 Voisin F., 2017, Environment Studies of Pulsar Wind Nebulae and Their Interactions with the Interstellar Medium  
 Voisin F., Rowell G., Burton M. G., Walsh A., Fukui Y., Aharonian F., 2016, MNRAS, 458, 2813  
 Weaver R., McCray R., Castor J., Shapiro P., Moore R., 1977, ApJ, 218, 377  
 de Jager O. C., Djannati-Ataï A., 2009, in Becker W., ed., Astrophysics and Space Science Library Vol. 357, Astrophysics and Space Science Library. p. 451 (arXiv:0803.0116), doi:10.1007/978-3-540-76965-1\_17

## APPENDIX A: NON-THERMAL EMISSION

This section will provide an overview of leptonic interactions and the subsequent photon emission via Synchrotron, Bremsstrahlung and inverse Compton Processes.

Synchrotron interactions occur when an electron interacts with background magnetic fields. The resulting SED emission from a single electron with Lorentz factor  $\gamma$  with pitch angle  $\alpha$  to the magnetic field  $B$  is given by:

$$P(\nu) = \frac{\sqrt{3}e^3 B}{mc^2} \frac{\nu}{\nu_c} \int_{\frac{\nu}{\nu_c}}^{\infty} K_{\frac{5}{3}}(x) dx \quad (\text{A1})$$

where  $e$  and  $m$  are the charge and mass of an electron respectively,

$K_{\frac{5}{3}}$  is the modified Bessel Function,  $\nu$  is the frequency of the gamma ray and  $\nu_c$  is the critical frequency of the emission:

$$\nu_c = \gamma^2 \frac{3eB \sin \alpha}{4\pi mc} \quad (\text{A2})$$

The inverse Compton gamma-ray SED from an electron with energy  $E_e$  scattering off a target photon with energy in range  $(\epsilon + d\epsilon)$  and number density  $n(\epsilon)$  can be found using:

$$\frac{dN}{dE_\gamma} = \frac{3\sigma_T mc^3}{4\gamma} \int_{E_\gamma/4\gamma^2}^{E_\gamma} \frac{n(\epsilon) d\epsilon}{\epsilon} f(q, \Gamma) \quad (\text{A3})$$

$$f(q, \Gamma) = 2q \ln q + (1 + 2q)(1 - q) + \frac{1}{2} \frac{(\Gamma q)^2}{1 + \Gamma q} (1 - q) \quad (\text{A4})$$

$$q = \frac{E_\gamma}{\Gamma(E_e - E_\gamma)}, \quad \Gamma = \frac{4\epsilon\gamma}{m_e c^2} \quad (\text{A5})$$

where  $\sigma_T = (3/8\pi)r_0^2$  is the Thompson cross section,  $r_0$  is the classical electron radius and  $F_{\text{KN}}$  takes account the full Klein-Nishina cross section for Inverse Compton scattering (Manolakou et al. 2007):

$$F_{\text{KN}} = \frac{1}{u_0} \int_0^\infty \ell(\gamma, \epsilon) u_\epsilon d\epsilon, \quad \ell(\gamma, \epsilon) = (1 + 4\gamma\epsilon)^{-\frac{3}{2}} \quad (\text{A6})$$

For a Planckian distribution of photon energies,  $F_{\text{KN}}$  can be approximated by:

$$F_{\text{KN}} = (1 + 4\gamma\epsilon_{\text{eff}})^{-3/2}, \quad \epsilon_{\text{eff}} = \frac{2.8kT}{m_e c^2} \quad (\text{A7})$$

Finally, the gamma-ray SED from Bremsstrahlung interactions is given by:

$$\frac{dN}{dE_\gamma} = nc \int d\sigma(E_e, E_\gamma, Z) dE_e \quad (\text{A8})$$

where  $Z$  is the atomic number of the target material and  $d\sigma$  is the bremsstrahlung differential cross section as defined in Blumenthal & Gould (1970).

The coefficients for leptonic losses in Equation 10 are:

- $b_s = 1.292 \times 10^{-15} (B/10^3 \mu\text{G})^2 \text{ s}^{-1}$  is the synchrotron loss coefficient
- $b_c = 1.491 \times 10^{-14} (n_H/1\text{cm}^{-3})$  is the Coulomb loss coefficient
- $b_b = 1.37 \times 10^{-16} (n_H/1\text{cm}^{-3}) \text{ s}^{-1}$  is the Bremsstrahlung loss coefficient
- $b_{\text{IC}} = 5.204 \times 10^{-20} (u_0/\text{eV}) \text{ s}^{-1}$  is the IC loss coefficient with the energy density of photons given by  $u_0$
- $n_H$  is the density of the ambient hydrogen gas

The diffusion radius for electrons (Atoyan et al. 1995):

$$R_{\text{diff}} = \sqrt{\frac{4D(\gamma)}{b_s \gamma (1 - \delta)} \left[ 1 - (1 - \gamma b_s t)^{1 - \delta} \right]} \quad (\text{A9})$$

## APPENDIX B: MAGNETIC FIELD DUE TO TURBULENT ISM GAS

The magnetic field due to the ISM gas with number density  $n$  is given through Crutcher's relation (Crutcher et al. 2010):

$$B_{\text{gas}}(n) = \begin{cases} B_{0,\text{gas}}, & n < 300 \text{ cm}^{-3} \\ B_{0,\text{gas}}(n/300 \text{ cm}^{-3})^\alpha, & n > 300 \text{ cm}^{-3} \end{cases} \quad (\text{B1})$$

where  $B_{0,\text{gas}} = 10 \mu\text{G}$  and  $\alpha = 0.65$ .

## APPENDIX C: SINGLE-ZONE MODELLING

Here we considered a 'single-zone' model, where single-zone modelling takes a region of constant number density and magnetic field and injects electrons into the centre (Sano et al. 2017; Collins et al. 2021). The final electron energy distribution in the region is found by solving Equation 1 by only considering radiative losses. The subsequent gamma-ray energy distribution is then estimated. While unable to encapsulate the complexity towards HESS J1825-137, a general insight of the system was gained before more detailed modelling of the morphology and time evolution.

### C1 Method

The Suzaku X-ray and HESS gamma-ray SED was extracted using two different areas by H.E.S.S. Collaboration et al. (2019) and Uchiyama et al. (2009) with radii  $r \approx 0.7$  and  $0.025$  respectively. Both regions were centered on the pulsar position. Consequently, the X-ray and gamma-ray emission must be modelled separately utilising single zone modelling.

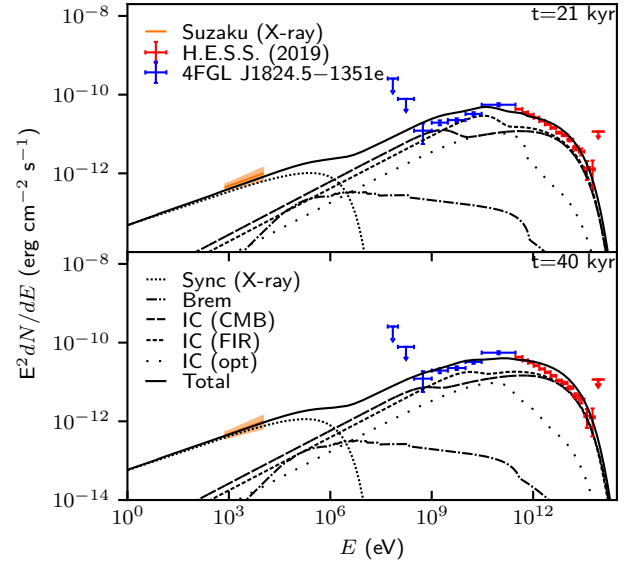
Supernovae tend to leave a bubble of low-density gas in the interstellar medium. Within the extent of the PWN, the density of both regions was set to  $0.5 \text{ cm}^{-3}$ . A diffusion coefficient of  $1.0 \times 10^{29} \text{ cm}^2 \text{ s}^{-1}$  was utilised, as proposed by H.E.S.S. Collaboration et al. (2019). Electrons were injected into the ISM at a constant rate  $\dot{E}$  and followed a power-law spectrum with an exponential cutoff:  $\frac{dN}{dE} \propto E^{-\Gamma} \cdot \exp(E/E_c)$ , where  $\Gamma$  is the spectral index and  $E_c$  is the cutoff energy. Two different ages were modelled, 21 kyr based on the characteristic age of the pulsar and 40 kyr based on previous modelling (Van Etten & Romani 2011).

The HESS region adopted a uniform magnetic field of  $5 \mu\text{G}$  as suggested by Principe et al. (2020) from comparing the estimated synchrotron emission to the Suzaku X-ray emission. Subsequently, it was assumed that the smaller X-ray region has a higher magnetic field strength than the HESS region due to the proximity of the pulsar and was left as a free parameter.

The fits to the SED towards HESS J1825-137 as well as the input parameters can be seen in Figure C1.

### C2 Discussion

Figure C1 shows the modelled SED with corresponding parameters to the gamma and X-ray spectra towards HESS J1825-137. The majority of gamma rays in this model are predicted to come from inverse Compton interactions from the infrared and CMB photon fields. An electron injection luminosity of  $2 \times 10^{38}$  and  $1 \times 10^{38} \text{ erg s}^{-1}$  is needed to match the gamma-ray spectra at ages 21 and 40 kyr respectively. This is a factor ten times greater than the spin-down power of PSR 1826-1334 ( $\dot{E} = 2.8 \times 10^{36} \text{ erg s}^{-1}$ ).



Parameter	$t = 21 \text{ kyr}$		$t = 40 \text{ kyr}$		units
	HESS	Suzaku	HESS	Suzaku	
$\dot{E}$	$2 \times 10^{38}$	$8 \times 10^{35}$	$1 \times 10^{38}$	$4 \times 10^{35}$	$\text{erg s}^{-1}$
$d$	4	4	4	4	kpc
$r$	0.70	0.025	0.70	0.025	
$n$	0.5	0.5	0.5	0.5	$\text{cm}^{-3}$
$B$	5	40	5	40	$\mu\text{G}$
$D_0$	$1 \times 10^{29}$	$1 \times 10^{29}$	$1 \times 10^{29}$	$1 \times 10^{29}$	$\text{cm}^2 \text{ s}^{-1}$
$\chi$	0.25	0.25	0.1	0.1	
$\Gamma$	2.1	1.9	2.1	1.9	
$E_c$	40	1000	50	1000	TeV

**Figure C1.** SED for leptonic interactions towards HESS J1825-137 using single-zone modelling. The X-ray and gamma-ray spectra are fitted separately due to the different coverage areas of HESS and Suzaku. The orange line shows the Suzaku match of X-rays between 1 – 9 keV towards the pulsar associated with HESS J1825-137 (Uchiyama et al. 2009). Blue data points represent the spectrum from the *Fermi*-LAT 4FGL source catalogue towards HESS J1825-137 while the red data shows the H.E.S.S. energy flux towards HESS J1825-137 (H.E.S.S. Collaboration et al. 2019). The top and bottom panels are at ages 21 kyr and 40 kyr respectively. The corresponding model parameters is shown in the table.

The single-zone model assumes a time-independent injection luminosity, whereas the spin-down power of the pulsar decreases over time. The spin-down power of PSR 1826-1334 could have been as high as  $10^{39} \text{ erg s}^{-1}$  at a pulsar age of 1 kyr (see § 3.1.2. Therefore the modeled injection luminosities represents the average electron injection luminosity over the age of the pulsar.

The X-ray emission towards PSR 1826-1334 can be predicted with an injection luminosity of  $8 \times 10^{35} \text{ erg s}^{-1}$  and  $4 \times 10^{35} \text{ erg s}^{-1}$  for the 21 and 40 kyr model respectively. The single-zone model can reasonably predict both the X-ray and gamma-ray SED, yet the X-ray and gamma-ray photon models require different injection spectra for both ages of the system. The single-zone model assumes constant density and magnetic field strength across the region of interest. However, the magnetic field structures towards PWNs have been suggested to be toroidal in nature but the viewing angle results in magnetic fields appearing radially dependent or tangled (Kotthes et al. 2006). If the dense clouds towards HESS J1826-130, as seen in Figure 2, lie at the same distance as the pulsar, diffusion will be suppressed towards this region with electrons losing their energy to bremsstrahlung losses. As previously mentioned, the spin-down power of the pulsar decreases over time which has an effect on the

injection luminosity of electrons in the ISM. While the single-zone model is able to predict the X-ray and gamma-ray SED towards HESS J1825-137, it is unable to encapsulate the complexity of the PWN.

#### APPENDIX D: DERIVATION OF PULSAR SPIN-DOWN POWER

Assuming there is no accretion of matter onto the pulsar, as the pulsar ages the angular frequency  $\Omega$  evolves according to:

$$\dot{\Omega} = -k\Omega^n \quad (\text{D1})$$

where  $n$  is the braking index of the pulsar and  $k$  is just a constant. Angular frequency is related to the period of the pulsar through  $\Omega = 2\pi P^{-1}$ , giving:

$$\dot{\Omega} = -\frac{2\pi}{P^2} \dot{P} \quad (\text{D2})$$

combining with Equation D1:

$$P^{n-2} \dot{P} = (2\pi)^{n-1} k = \text{constant} \quad (\text{D3})$$

$$\therefore \dot{P}_0 P_0^{n-2} = \dot{P}(t) P^{n-2}(t) = \dot{P}_{\text{age}} P_{\text{age}}^{n-2} \quad (\text{D4})$$

where  $P_0 = P(0)$  and  $P_{\text{age}} = P(t_{\text{age}})$ . Integrating Equation D3 from time  $t$  to the current age of the pulsar  $t_{\text{age}}$ :

$$\int_t^{t_{\text{age}}} P^{n-2} \frac{dP}{dt} dt = \int_t^{t_{\text{age}}} (2\pi)^{n-1} k dt \quad (\text{D5})$$

$$\int_{P(t)}^{P_{\text{age}}} P^{n-2} dP = \int_t^{t_{\text{age}}} (2\pi)^{n-1} k dt \quad (\text{D6})$$

Assuming  $n \geq 2$ :

$$P^{n-1}(t) = -(n-1) \left[ (2\pi)^{n-1} k \right] (t_{\text{age}} - t) + P_{\text{age}}^{n-1} \quad (\text{D7})$$

Utilising Equation D4:

$$P(t) = P_{\text{age}} \left[ 1 - (n-1) \frac{\dot{P}_{\text{age}}}{P_{\text{age}}} (t_{\text{age}} - t) \right]^{n-1} \quad (\text{D8})$$

The rotational energy of pulsar,  $E_{\text{rot}}$  is related to its angular frequency:

$$E_{\text{rot}} = \frac{1}{2} m r^2 \Omega_{\text{age}}^2 = \frac{1}{2} m r^2 \frac{(2\pi)^2}{P_{\text{age}}^2} \quad (\text{D9})$$

where  $m$  and  $r$  are the mass and radius of the pulsar respectively. Therefore the spin-down of the pulsar can be described by

$$\dot{E}(t) = \frac{1}{2} m r^2 (2\pi)^2 (-2) \frac{\dot{P}(t)}{P^3(t)} \quad (\text{D10})$$

leading to:

$$\dot{E}(t) = \dot{E}_{\text{age}} \left( \frac{P_{\text{age}}}{P(t)} \right)^{n+1} \quad (\text{D11})$$

Combining Equation D8 and Equation D11:

$$\dot{E}(t) = \dot{E}(t_{\text{age}}) \left[ 1 + (n-1) \frac{\dot{P}(t - t_{\text{age}})}{P} \right]^{-\Gamma_n} \quad (\text{D12})$$

where:

$$\Gamma_n = \frac{n+1}{n-1} \quad (\text{D13})$$

Note that a caveat to Equation D12 is that:

$$n \leq 1 - \frac{P}{\dot{P}(t - t_{\text{age}})} \quad (\text{D14})$$

Therefore for an age of 21 kyr, PSR J18226-130 requires that  $n \leq 3.03$  and for an age of 40 kyr,  $n \leq 2.07$ .

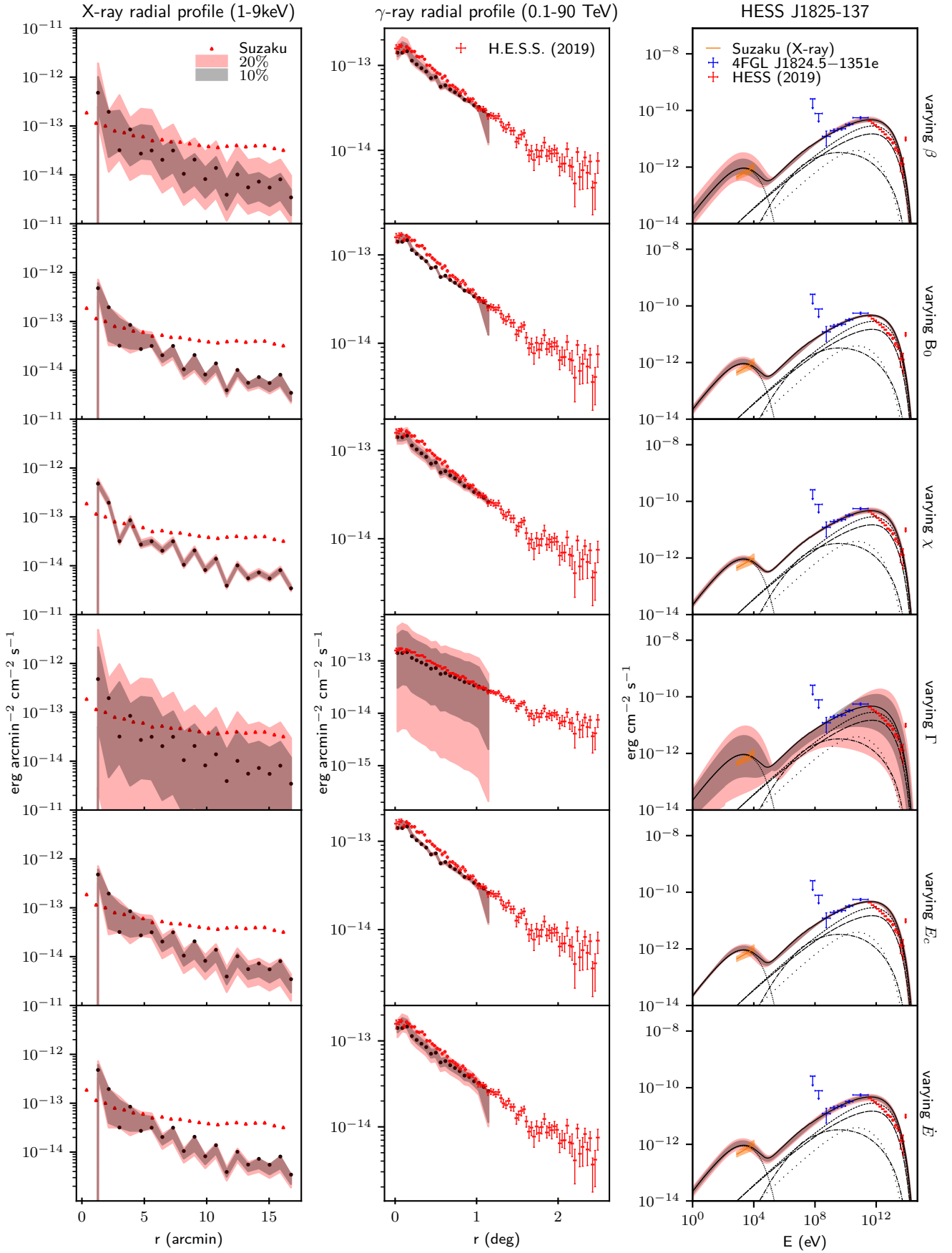
#### APPENDIX E: SYSTEMATIC VARIATION OF MULTIZONE PARAMETERS

Figure E1 and Figure E2 shows the 10% and 20% systematic variation of the free parameters,  $\dot{E}$ ,  $\chi$ ,  $\gamma$ ,  $E_c$ ,  $B_0$  and  $\beta$  for the 21 kyr and 40 kyr models. These figures show that the spectral index of injection electrons,  $\Gamma$ , exerts the most influence on the SED and radial profiles than  $\chi$ ,  $B_0$  and  $\beta$ . The X-ray SED and radial profiles are more sensitive on the parameters than the gamma-ray emission. This is a result of the smaller region used to extract the X-ray and SED (see Figure 2 and Figure 4).

The modelled X-ray radial profiles for the 21 and 40 kyr models are steeper than observations (Uchiyama et al. 2009) indicating that the model over-predicts the synchrotron emission closer to PSR 1826-1334. This may be corrected by decreasing the rate at which the magnetic field drops off with distance from the pulsar ( $\beta$ ), allowing electrons to escape the PWN at a faster rate. The outer edges of the PWN experiences greater synchrotron losses at the cost of TeV gamma-ray emission from IC interactions, flattening out the gamma-ray radial profile. This is demonstrated in the 10 and 20% variation of  $\beta$  shown in the top row of Figure E1 and Figure E2. Alternatively, decreasing the overall magnetic field strength,  $B_0$ , decreases synchrotron losses towards HESS J1825-137 at the cost of increasing the gamma-ray to X-ray flux ratio. With flux being dependent on the observational area, any changes to the gamma-ray and X-ray ratio will be more prominent in the X-ray SED as shown in Figure E1 and Figure E2.

To better fit the X-ray radial profile, the diffusion suppression coefficient towards HESS J1825-137 could be increased to allow electrons to escape further from the pulsar before losing their energy to synchrotron radiation. High-energy electrons rapidly lose their energy to radiative losses and remain close to the pulsar, hence the gamma-ray radial profile will flatten as shown in Figure E1 and Figure E2. As the region used to extract the X-ray data is small ( $< 2pc$ ) compared to the HESS region ( $\approx 49 pc$ ), electrons quickly escape the X-ray region while remaining in the HESS region. Thus the X-ray SED far more sensitive to the value of  $\chi$  than the gamma-ray SED.

Both the radial profiles and SED are very sensitive to the injected electron spectral index,  $\Gamma$ , as seen in Figure E1 and Figure E2. If  $\beta$ ,  $B_0$  or  $\chi$  was altered to fit the observed Suzaku X-ray radial profile, the predicted SED from the model will no longer fit to the data. In turn, the spectral index can be modified to refit the modelled SED. Consequently, the X-ray radial profile will no longer match the Suzaku observations.



**Figure E1.** 21 kyr Model 1 as in Figure 4 but with 10% (grey shaded band) and 20% (pink shaded band) variation in parameters.



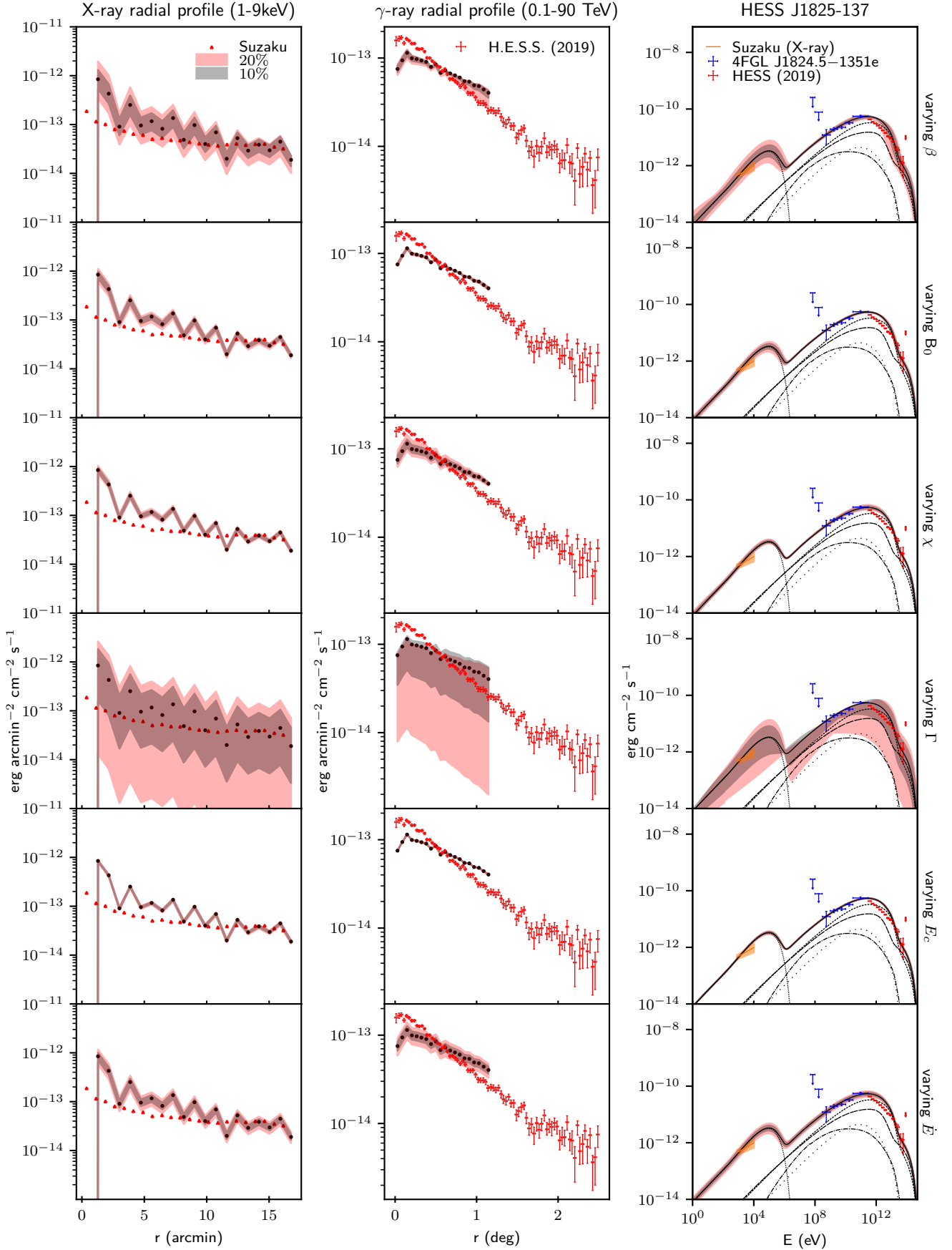


**Figure E2.** 40 kyr Model 2 as in Figure 5 but with 10% (grey shaded band) and 20% (pink shaded band) variation in parameters.

The cutoff energies for the 21 kyr and 40 kyr models are 45 TeV and 500 TeV respectively. As the cutoff energy for an exponential cutoff power-law increases, the energy spectra starts to follow a power-law. Hence, the systematic variation of  $E_C$  is less apparent for 40 kyr than 21 kyr as seen in the fourth row of Figure E1 and Figure E2 respectively.

## APPENDIX F: ADDITIONAL FIGURES

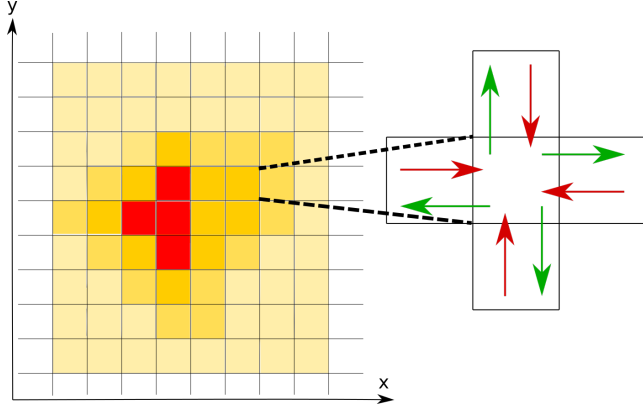


Figure F1: A 2D representation of the 3D grid used to numerically solve the transport equation (Equation 1). The zoomed in cell shows the flux of electrons in (red) and out (green) of the cell in one time step  $\Delta t$ .

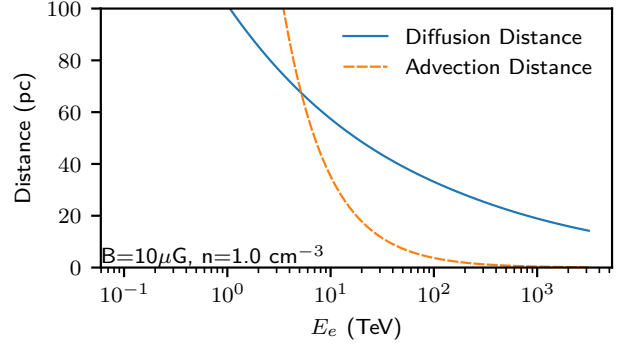


Figure F4: The distance that electrons are transported before losing their energy through radiative cooling (synchrotron, inverse Compton and Bremsstrahlung) assuming purely diffusive (solid line) or advective transport (dashed line).

This paper has been typeset from a  $\text{\LaTeX}$  file prepared by the author.

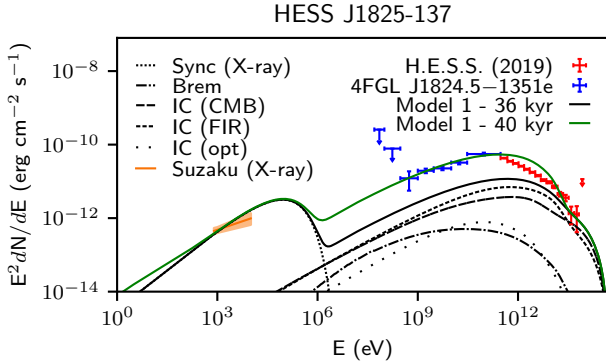


Figure F2: Total SED for a system of age 36 kyr Model 1 shown in green vs the 40 kyr Model 1 shown in Figure 5. The 36 kyr model has the same parameters as the 40 kyr model.

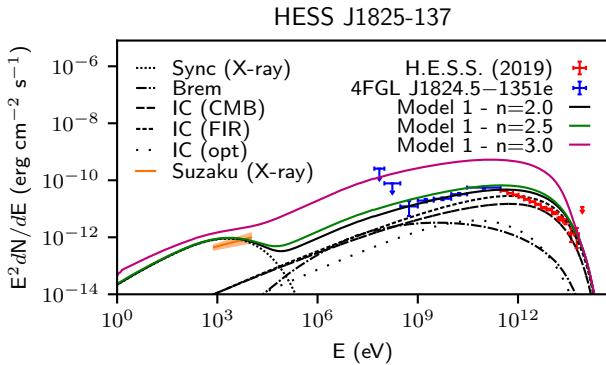
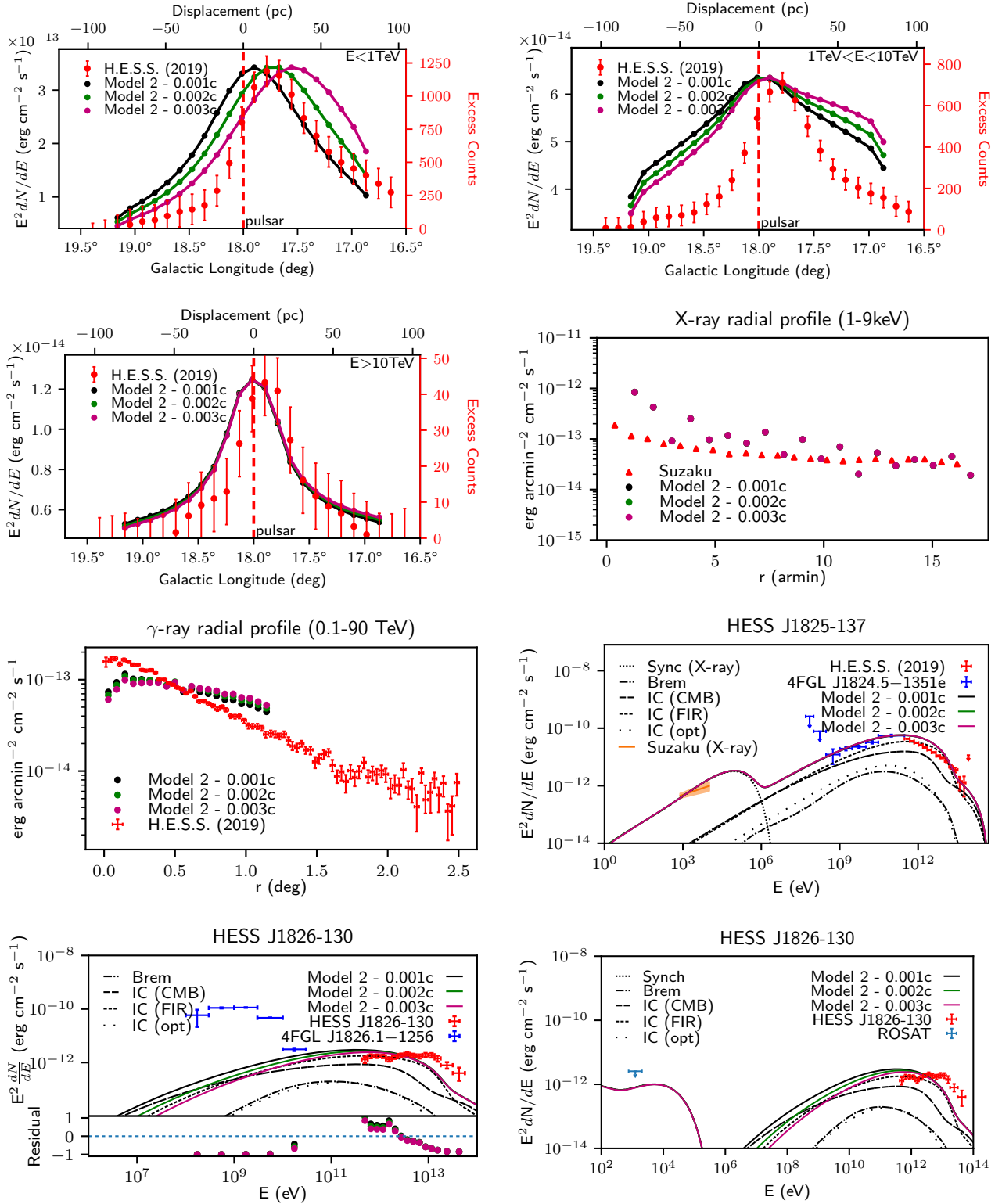


Figure F3: Total SED for a system with the same parameters as the 21 kyr Model 1 but with  $n = 2.0$  (black),  $n = 2.5$  (green) and  $n = 3.0$  (purple).



**Figure F5.** Comparison of Model 2 with an advective flow velocity of  $0.001c$  (black),  $0.002c$  (green) and  $0.003c$  (purple)